Gamma-Ray Burst Jet Profiles And Their Signatures

C. Graziani, D. Q. Lamb, and T. Q. Donaghy

carlo@oddjob.uchicago.edu, quinn@oddjob.uchicago.edu, lamb@oddjob.uchicago.edu

Department of Astronomy and Astrophysics, University of Chicago, 5640 S. Ellis Avenue, Chicago, IL 60637

ABSTRACT

HETE-II and BeppoSAX have produced a sample of GRBs and XRFs with known redshifts and E_{pk}. This sample provides four important empirical constraints on the nature of the source jets: Log E_{iso} is approximately uniformly distributed over several orders of magnitude; the inferred prompt energy Log E_γ is narrowly distributed; the Amati relation holds between E_{iso} and E_{pk}; and the Ghirlanda relation holds between E_γ and E_{pk}.

We explore the implications of these constraints for GRB jet structure during the prompt emission phase. We infer the underlying angular profiles from the first two of the above constraints assuming all jets have the same profile and total energy, and show that such "universal jet" models cannot satisfy both constraints.

We introduce a general and efficient method for calculating relativistic emission distributions and E_{pk} distributions from jets with arbitrary (smooth) angular jet profiles. We also exhibit explicit analytical formulas for emission from top-hat jets (which are not smooth). We use these methods to exhibit E_{pk} and E_{iso} as a function of viewing angle, for several interesting families of GRB jet profiles. We use the same methods to calculate expected frequency distributions of E_{iso} and E_γ for the same families of models.

We then proceed to explore the behavior of universal jet models under a range of profile shapes and parameters, to map the extent to which these models can conform to the above four empirical constraints.

Subject headings: Gamma Rays: Bursts — ISM: Jets and Outflows — Shock Waves

1.   Introduction

Since the recognition that gamma-ray burst (GRB) sources are highly relativistic collimated jets, the study of the structure of the jets and of the distribution of jet parameters

among burst sources has been an area of active research. An early observational success of the jet picture of GRBs was the discovery by Frail et al. (2001) of a striking correlation between GRB energy fluence and the break times of GRB afterglow light curves. Using the simple picture of a conical, uniform jet, Frail et al. (2001), and later Bloom et al. (2003) inferred jet opening angles from the break times using results on the dynamics of afterglows of Sari et al. (1999) for a sample of GRBs with known redshifts. After correcting the isotropic-equivalent gamma-ray energy of each GRB by the inferred solid angle subtended by its conical jet, Frail et al. (2001) found that the extremely broad (3-4 decades) distribution of isotropic-equivalent energy was mapped to a remarkably narrow (~ 1 decade) distribution of inferred total energy.

The debate over the meaning of this result has given rise to two main alternative interpretations. The first interpretation is an elaboration of that of Frail et al. (2001), in which GRB sources all have a common amount of energy available for gamma-ray emission (they are "standard bombs"), and differ from one another by the opening angle of their conical jet (Lamb, Donaghy, & Graziani 2005). Implicit in this view is that little or no emission is received by an observer whose line-of-sight is not included in the jet cone.

The alternative view is that GRB jets might have structure that is richer than a simple uniformly-emitting cone. The attractive feature of this picture is that if the jet structure is sufficiently rich, it might be possible to ascribe the same jet structure to all GRB jets, and to explain the distribution of GRB energies using only the variation of observer lines-of-sight with respect to the jet axis (Rossi et al. 2002; Zhang & Mészáros 2002).

These two viewpoints are sometimes presented juxtaposed as the "uniform jet model" and the "structured jet model". This terminology is unfortunate, since it is clear that the real distinction under debate is not really whether GRB jets have "structure", but rather whether the observed energetics of GRBs can be explained in terms of a single parameter (the angle between the observer's line-of-sight and the jet axis), or whether additional parameters relating to jet structure are required. Thus the juxtaposition would be better thought of as the "universal jet model" versus the "variable-geometry jet model," where a sort of middle ground is occupied by the "quasi-universal model" (Lloyd-Ronning et al. 2004).

One element that has not featured prominently in discussions of jet structure is the role of relativistic kinematics in prompt GRB emission. Relativistic kinematics is a central feature of the "off-axis beaming" models of Yamazaki and collaborators (Yamazaki et al. 2002, 2003, 2004; Toma et al. 2005), which those authors used to attempt to unify the phenomenon of GRBs with that of "X-Ray Flashes" or XRFs (Heise et al. 2001; Kippen et al. 2001). However, their models invoke a uniform conical "top-hat" jet structure. By and large, calculations of prompt emission expected from "structured" jets have essentially

bypassed the role of relativistic beaming and Doppler shift, assuming a "what you see is what you get" relation of the jet emission profile to the jet radiation pattern that tacitly implies a Lorentz factor satisfying $\gamma^{-1} \to 0$ (Zhang & Mészáros 2002; Lloyd-Ronning et al. 2004; Zhang et al. 2004).

This is a gap that is worth plugging. It is clear that the observed radiation pattern from a "structured" GRB jet can be substantially modified by relativistic kinematics, both spectrally and in terms of total radiated energy. Depending on the Lorentz factor and viewing angle, relativistic kinematics can turn a steep jet profile into a shallow radiation pattern, or turn a hard source spectrum into a soft observed spectrum (or, as we shall see, vice versa). It is certainly not safe to assume that it is even possible to produce a given radiation pattern without a stringent — and possibly unphysical — constraints on the Lorentz factor.

Certain constraints on universal jet shapes and distributions may be inferred from observations. The empirical constraints on jet models that we consider here are illustrated in Fig. 1. They are:

- The distribution of GRB isotropic-equivalent energy E_{iso} appears to be quite broad, spanning at least four orders of magnitude, and appears approximately uniform in $\log E_{\mathrm{iso}}$, that is,

$$dN/d\log E_{\mathrm{iso}} \approx A, \tag{1}$$

  where A is a constant (Amati et al. 2002; Lamb et al. 2004).

- The distribution of GRB total gamma-ray energy inferred using the Frail et al. (2001) procedure — $E_\gamma^{(\mathrm{I})}$ — appears to be quite narrow, with most values clustered within a decade around a geometric mean whose (model-dependent) value is somewhere in the range 5×10^{50}–3×10^{51} erg (Frail et al. 2001).

- Empirically, GRB isotropic energies E_{iso} and peak energies E_{peak} of GRB νF_ν spectra appear to be satisfy the "Amati Relation", a very tight correlation according to which $E_{\mathrm{peak}} \sim E_{\mathrm{iso}}^{1/2}$ (Amati et al. 2002; Lamb et al. 2004).

- Empirically, GRB inferred total energies $E_\gamma^{(\mathrm{I})}$ and peak energies E_{peak} of GRB νF_ν spectra appear to be satisfy the "Ghirlanda Relation", a very tight correlation according to which $E_{\mathrm{peak}} \sim E_\gamma^{(\mathrm{I})\,0.7}$ (Ghirlanda et al. 2004).

In this paper we consider the extent to which universal jet models with various underlying emission profiles can satisfy these observational constraints on GRBs with afterglows and redshifts. The plan of the paper is as follows:

In §2 we consider the effect of the choice of functional form of the emission profile on the frequency distributions of E_{iso} and $E_\gamma^{(\mathrm{I})}$. We consider power-law profiles, and introduce the "Fisher" (exponential) profile, which is designed to satisfy Eq. (1) exactly. We also inquire into the distributional properties of top-hat jet profiles in universal jet models.

The treatment in §2 uses "bare" emission, that is, uncorrected by relativistic kinematics. In §3 we introduce a general and efficient method of computing fully relativistic prompt emission from jets with arbitrary (smooth) emission profiles. We introduce the notion of "photon-number-weighted average Doppler shift", a quantity that serves as a proxy for observed E_{peak}. We also exhibit the method for calculating how the frequency distributions of §2 are modified by relativistic kinematics. Finally, we give compact analytic expressions for relativistically-correct emission and average Doppler factor in the special case of the top-hat jet profile.

In §4, we use these ideas to explore the characteristic angular emission profiles, E_{iso}-E_{peak} ("Amati"), and $E_\gamma^{(\mathrm{I})}$-E_{peak} ("Ghirlanda") relations that would be observed from Universal GRB models with Fisher, power-law, and top-hat emission profiles. We also show explicitly how the frequency distributions of §2 are modified by relativistic kinematics.

Our conclusions concerning the ability of universal jets based on the various emission profiles to satisfy the observational constraints are discussed in §5

2. Universal Jet Profiles and Their Frequency Distributions in Energy

For the sake of clarity of the discussion that follows, it is useful to draw a terminological distinction between jet profiles and jet models.

A jet *profile* is a distribution of emission across the surface of the emitting shock. Popular choices include the "top hat" jet, and $\theta^{-\delta}$ power-laws of Rossi et al. (2002) and Zhang & Mészáros (2002) (also sometimes referred to as the "structured jet"), where θ denotes angular location on the jet.

A jet *model* of GRB emission includes a choice of profile, but also a choice of distribution of profile parameters. For example, the model of Zhang & Mészáros (2002) selects a power-law with a fixed index, and a fixed total energy. The "Variable Opening Angle" model of Lamb, Donaghy, & Graziani (2005), on the other hand, selects a top-hat profile and assumes a fixed total energy, but a distribution of jet opening angles.

Models such as that of Rossi et al. (2002) and Zhang & Mészáros (2002) that adopt a fixed profile shape and total prompt energy — and thus rely only on the variation of

observer viewing angle to produce all the distributions of GRB energetics — are properly called "universal" models. We will refer to models that allow for variations in profile shape as "variable-geometry" models. Note that neither class of models necessarily requires that its underlying profile should belong to a particular family — one can in principle "mix-and-match" models and profiles quite freely.

It is apparent that universal-jet models of GRBs are simpler than variable-geometry models, in the sense that they require fewer parameters. Clearly, an important question that must be addressed in this connection is: do universal jet models have enough freedom to satisfy known observational constraints on GRBs? This question is the main concern of this paper.

As a notational preliminary, let $X_{\rm iso} \equiv \ln E_{\rm iso}$, and $\mu_v \equiv (1 - \cos \theta_v)$, where θ_v is the angle between the line-of-sight and the center of the jet. We will also use $X_\gamma^{\rm (T)} \equiv \ln E_\gamma^{\rm (T)}$ and $X_\gamma^{\rm (I)} \equiv \ln E_\gamma^{\rm (I)}$, where "(T)" refers to "True" (i.e. the actual total gamma-ray energy emitted), and "(I)" refers to "Inferred" — the gamma-ray energy inferred using the Frail et al. (2001) procedure, in which the jet energy is corrected from its "isotropic" value using the solid angle subtended by the jet opening angle inferred from the break time of the jet. In general, $E_\gamma^{\rm (I)} \neq E_\gamma^{\rm (T)}$.

In this section, we assume symmetric "2-lobed" jets, so that $0 < \mu_v < 1$.

2.1. The Fisher Jet Profile

Suppose we describe a Universal Jet by a function $f(\mu_v)$, that is

$$X_{\rm iso} = f(\mu_v). \tag{2}$$

How do we choose $f(\mu_v)$ so as to satisfy the constraint of Eq. (1)?

By construction, Universal jet models assume all properties of GRB energetics are produced by variation of the viewing angle. Naturally, this variation is assumed uniform in μ_v for $0 < \mu_v < 1$. In this range of μ_v, we therefore have

$$\begin{aligned} \frac{dN}{dX_{\rm iso}} &= \frac{dN/d\mu_v}{dX_{\rm iso}/d\mu_v} \\ &= B\left[f'(\mu_v)\right]^{-1}\big|_{f(\mu_v)=X_{\rm iso}}, \end{aligned} \tag{3}$$

where B is an uninteresting normalization constant. This kind of expression corresponds closely to expressions of Guetta et al. (2005) concerning universal jet models, the obvious

difference being that here we concern ourselves with modeling the E_{iso} distribution, and not the observed fluence distribution.

In consequence of the limited allowed range of μ_v, dN/dX_{iso} can only be constant in a limited range of X_{iso}. Within that range, we have $f'(\mu_v) = \text{const.}$, so that

$$X_{\text{iso}} = f(\mu_v) = c_1\mu_v + c_0, \tag{4}$$

and

$$\frac{dN}{dX_{\text{iso}}} = \frac{1}{c_1}\Theta(X_{\text{iso}} - c_0)\Theta(c_0 + c_1 - X_{\text{iso}}). \tag{5}$$

The shape of the jet in linear energy space is

$$E_{\text{iso}} = \exp(c_1\mu_v + c_0), \tag{6}$$

which peaks at $\mu_v = 1$ for $c_1 > 0$. The larger c_1, the sharper the peak. This functional form is called the "Fisher Distribution", and is well known from the theory of statistical distributions on spheres (Mardia 1972, p.228). In the small-angle approximation, when $\mu_v \approx (1-\theta_v^2/2)$, it approaches a symmetric 2-dimensional Gaussian with standard deviation $\theta_0 \equiv c_1^{-1/2}$, a form considered by Zhang & Mészáros (2002), Zhang et al. (2004), Lloyd-Ronning et al. (2004), and Dai & Zhang (2005). The Fisher distribution is more convenient for our purposes, since its geometrically-natural form makes it useful for analytical work for widths and viewing angles well outside the small-angle approximation.

Note that the domain restriction in Eq. (5) says that X_{iso} varies over a domain whose breadth is $c_1 = 1/\theta_0^2$. For a jet with an opening angle of 5.7°, $\theta_0 = 0.1$, and the resulting range of E_{iso} is 100 e-foldings, corresponding to about 43 decades. Naturally, instrument thresholds prevent us from probing such a range of E_{iso}.

It is convenient to adjust the normalization of this expression so that it reflects the true emitted energy, $E_\gamma^{(\text{T})}$. Since $E_{\text{iso}} = 4\pi dE_\gamma^{(\text{T})}/d^2\Omega_v$, we have

$$
\begin{aligned}
E_\gamma^{(\text{T})} &= 2\int_0^1 \frac{1}{2}d\mu_v\, e^{\mu_v/\theta_0^2 + c_0} \\
&= e^{c_0}\theta_0^2\left(\exp(\theta_0^{-2}) - 1\right),
\end{aligned}
\tag{7}
$$

where the factor of 2 in the first line accounts for the energy in both lobes of the symmetric jet.

We thus have

$$E_{\text{iso}} = \frac{E_\gamma^{(\text{T})}}{\theta_0^2\left(\exp(\theta_0^{-2}) - 1\right)}e^{\mu_v/\theta_0^2}, \tag{8}$$

and

$$
\begin{aligned}
X_{\text{iso}} &= X_\gamma^{(\text{T})} + \theta_0{}^{-2}\mu_v - \ln\left[\theta_0{}^2\left(\exp(\theta_0{}^{-2})-1\right)\right] \\
&\approx X_\gamma^{(\text{T})} - \theta_0{}^{-2}(1-\mu_v) + \ln\theta_0{}^{-2},
\end{aligned}
\tag{9}
$$

where in the final line we have made the approximation $\theta_0{}^2 \ll 1$.

2.2. The $X_\gamma^{(\text{I})}$ Distribution of Universal Fisher Jets

The quantity E_{iso} is directly related to a physical property of the GRB — the energy emitted per unit solid angle along the observer's line-of-sight. The quantity $E_\gamma^{(\text{I})}$, on the other hand, has a slightly different status. It is the result of a data-analysis procedure — the Frail et al. (2001) procedure — which multiplies E_{iso} by a solid angle interior to a jet opening angle inferred from the light-curve break time. This procedure is particularly adapted to top-hat profile jets, so the physical meaning of $E_\gamma^{(\text{I})}$ in the context of other profiles can be somewhat contrived. Nonetheless, the empirical distribution of $E_\gamma^{(\text{I})}$ appears to supply important constraints on jet models, as noted above, so it is important to understand jet model predictions of these distributions.

In the case of top-hat jet profiles, the Frail et al. (2001) procedure infers a jet opening angle from the afterglow light-curve break time. In the case of a non-uniform universal jet, the break time does not correspond to a jet edge. Rather, it occurs when the bulk of the emission from the jet is accessible to the observer, since after that time, the evolution of the light curve is controlled by the evolution of γ only, which is expected to be a power-law in time.

As pointed out by Kumar & Granot (2003) and Dai & Zhang (2005), the light-curve break indicates one of two situations: (1) the viewing angle θ_v is larger than θ_0, and the beaming angle $1/\gamma$ has widened to the point that the *peak* of the jet has become visible, so that the emission can no longer increase in brightness at the rate that it did when the beaming cone was still climbing up the peak. Or (2) the viewing angle θ_v is smaller than θ_0, and the beaming angle $1/\gamma$ has widened until it is equal to θ_0, so that most of the jet emission is now visible, and further increase in $1/\gamma$ produces a diminishing return in flux.

Following Kumar & Granot (2003) and Dai & Zhang (2005), we therefore assume that the inferred break angle $\theta_{br} = \max(\theta_v, \theta_0)$, and that $E_\gamma^{(\text{I})}$ is given by

$$
E_\gamma^{(\text{I})} = E_{\text{iso}} \times (1 - \mu_{br}),
\tag{10}
$$

where $\mu_{br} \equiv \cos\theta_{br}$

We may now inquire as to the distribution $dN/dX_\gamma^{(I)}$ of Universal Fisher jets. $X_\gamma^{(I)}$ is given by

$$X_\gamma^{(I)} = X_{\text{iso}} + \ln(1 - \mu_{br}). \tag{11}$$

The shape of this function is shown in Fig. 2. From the figure, it is apparent that the range of $E_\gamma^{(I)}$ is about the same as the range of E_{iso}, about $\exp(\theta_0^{-2})$. It also appears that the correspondence from $X_\gamma^{(I)}$ to μ_v is single-valued in almost all of this range, except for an small annulus of inner radius θ_0 and outer radius $\sqrt{2}\theta_0$, where it is three-valued.

We may therefore write

$$
\begin{aligned}
\frac{dN}{dX_\gamma^{(I)}} &= \sum_{\text{Roots}} \frac{dN/d\mu_v}{dX_\gamma^{(I)}/d\mu_v} \\
&= B \times \sum_{\text{Roots}} \left| \theta_0^{-2} - \frac{1}{1 - \mu_v} \right|^{-1} \Bigg|_{X_\gamma^{(I)} = X_{\text{iso}}(\mu_v) + \ln(1 - \mu_{br})},
\end{aligned}
\tag{12}
$$

where the sum is over the roots of Eq. (11), of which there is only one outside the aforementioned annulus.

Assuming a typical $\theta_0 \lesssim 0.1$, it is apparent that in most of the range $0 < \mu_v < 1$, the first term in the summand of Eq. (12) dominates the second term, so that $dN/dX_\gamma^{(I)}$ is approximately also uniform in most of its range. It does spike (integrably) when $1 - \mu_v = \theta_0^2$ (as θ_v crosses the inner radius of the annulus), but this behavior is not enough to make the distribution a narrow one. Most of the probability, and therefore most of the events, occur at a range of angles considerably larger than the core annulus, which subtends a small solid angle. For example, the 95% point of the $dN/dX_\gamma^{(I)}$ distribution occurs at a value of $X_\gamma^{(I)}$ corresponding to $\mu_v = 0.05$. With $\theta_0^{-2} = 100$, this value of $X_\gamma^{(I)}$ is lower than the value near the jet core by about 90 e-foldings, equivalent to about 39 decades. Examples of the behavior of Eq. (12) are shown by the "bare" cuves in the four panels of Fig. 9, for a range of values of θ_0.

We see that Eq. (12) represents an extremely broad distribution, far broader than can actually be probed by real instruments – obviously, HETE, BeppoSAX, BATSE and SWIFT didn't and won't probe 40 decades of $E_\gamma^{(I)}$ or E_{iso}. The key point, however, is that in the observationally accessible region, the distribution is broad, not narrow, and is only cut off by instrumental effects.

2.3.   The $X_{\rm iso}$ Distribution of "Universal Structured" Jets

The universal "structured" jet model of Rossi et al. (2002) and Zhang & Mészáros (2002) does not attempt to satisfy constraint (1). Instead, it attempts to preserve the appearance of the Frail et al. (2001) result — that is, to satisfy constraint

$$dN/dX_\gamma^{(I)} = N_0 \times \delta(X_\gamma^{(I)} - \bar{X}_\gamma^{(I)}). \tag{13}$$

by imposing the following shape:

$$E_{\rm iso} = K/(1 - \mu_v), \tag{14}$$

or, equivalently,

$$X_{\rm iso} = Q - \ln(1 - \mu_v), \tag{15}$$

where K and Q are constants, and where we have replaced the small-angle form with the general, spherically-correct form.

Since this form does not attempt to constrain $dN/dX_{\rm iso}$, it is of interest to calculate what this distribution might be. This is easily done:

$$
\begin{aligned}
\frac{dN}{dX_{\rm iso}} &= \frac{dN/d\mu_v}{dX_{\rm iso}/d\mu_v} \times \Theta(X_{\rm iso} - Q) \\
&= B \times (1 - \mu_v) \times \Theta(X_{\rm iso} - Q) \\
&= (BK/E_{\rm iso}) \times \Theta(X_{\rm iso} - Q) \\
&= BKe^{-X_{\rm iso}} \times \Theta(X_{\rm iso} - Q).
\end{aligned}
\tag{16}
$$

In other words, the distribution is exponential in $X_{\rm iso}$, with a width scale of one e-folding (0.43 decades) and a cutoff at some low value of $X_{\rm iso}$. Needless to say, the empirical distribution (Fig. 1) looks nothing like this.

2.4.   Jet Distributions, Broad and Narrow

It appears from the foregoing that universal jet models have a serious problem: if you try to make a jet that has a broad $E_{\rm iso}$ distribution, you find that the jet also has a broad $E_\gamma^{(I)}$ distribution, while forcing a narrow $E_\gamma^{(I)}$ distribution results in a narrow $E_{\rm iso}$ distribution.

To illustrate the point, suppose we let the functional relation between $E_{\rm iso}$ and 1-μ_v be a general power-law, so that

$$X_{\rm iso} = Q - \delta \ln(1 - \mu_v). \tag{17}$$

The universal "structured" jet model of Rossi et al. (2002) and Zhang & Mészáros (2002) corresponds to $\delta = 1$. Those authors also considered general power-law jet profiles as well, although those profiles were power-laws in θ_v, rather than in the solid angle interior to θ_v as here.

It then follows, by the same argument that led to Eq. (16), that the energy distributions are:

$$\frac{dN}{dX_{\mathrm{iso}}} = C \times \delta^{-1} e^{-X_{\mathrm{iso}}/\delta} \times \Theta(X_{\mathrm{iso}} - Q), \tag{18}$$

and

$$\frac{dN}{dX_\gamma^{(\mathrm{I})}} = C \times (\delta - 1)^{-1} e^{-X_\gamma^{(\mathrm{I})}/(\delta-1)} \times \Theta(X_\gamma^{(\mathrm{I})} - Q). \tag{19}$$

Note that for the Zhang & Mészáros (2002) universal jet profile, $\delta \to 1$, and the right-hand side of Eq. (19) tends to a δ-function.

It appears from Eqs. (18) and (19) that the family of models satisfying Eq. (17) is capable of producing energy distributions of any breadth, simply by varying the value of δ. The larger the value of δ, the broader the distribution. This property is in contrast with the properties of Fisher jets, which (by design) can only represent broad E_{iso} distributions. We may therefore use the power-law jet family of models to explore the connection between the breadth of the X_{iso} distribution and that of the $X_\gamma^{(\mathrm{I})}$ distribution.

From Eqs. (18) and (19) we may observe that within this family of models, the widths of the two distributions are closely linked: if we try to push out the width of the X_{iso} distribution by increasing δ, we will also automatically increase the width of the $X_\gamma^{(\mathrm{I})}$ distribution to very nearly the same width. If, on the other hand, we attempt to restrict the range of $X_\gamma^{(\mathrm{I})}$ by making δ close to 1, we thereby also restrict the range of X_{iso}.

It appears, then, that Universal jet models *force us to choose between two observational constraints on GRBs.* Within the context of a universal jet model, it is not possible to satisfy both the requirement that dN/dX_{iso} should be broad and the requirement that $dN/dX_\gamma^{(\mathrm{I})}$ should be narrow.

3. Computing Relativistic Emission From Jet Profiles

In this section we present formulas and methods of computing various observational quantities given certain jet angular emission profiles. Naturally, underlying emission profiles are not observed directly, but rather they are modulated by relativistic effects due to their relativistic bulk motion.

In this work, we are concerned with jet emission profiles that are due to variations in emissivity across the jet, rather than due to variations in the Lorentz factor γ. We consider that during the prompt emission phase of the GRB, γ is constant across the jet and has no appreciable time variation (Rees & Mészáros 1994).

We consider prompt energies and observed fluences, rather than prompt peak luminosities and observed peak fluxes. Given the assumed invariance of γ, this approach allows us to ignore time variations in the emission, and to represent prompt emission properties of GRBs simply in terms of weighted integrals of jet angular profiles.

We also assume that the observer's detection process is approximately bolometric — that is, we ignore the spectral effects of relativistic kinematics, so we do not concern ourselves with the kinematic transformations of detector bandpasses, or with the integration of emission spectra over those bandpasses.

Note that in this section, unlike in §2, we assume "single-lobed" jets, for the sake of simplicity of our expressions. A symmetric "two-lobed" jet may be constructed from oppositely directed single-lobed jets, ascribing half of the total energy to each lobe.

3.1. Observables

3.1.1. E_{iso} and $E_\gamma^{(I)}$

It is obviously of interest to calculate the observed fluence as a function of viewing angle, from which $E_{\rm iso}$ follows directly.

In what follows, we refer to the inertial frame at rest with respect to an element of the jet as the "rest frame" (of that element), and to the inertial frame at rest with respect to the central engine as the "source frame."

Suppose a jet with bulk Lorentz factor γ radiates a source-frame energy $E_\gamma^{(\rm T)}$. Let each differential element of the jet $d^2\vec{n}$ be labeled by the unit vector $\vec{n}$, so that $\vec{n}$ furnishes coordinates on the jet surface. For concreteness, we will assume $\vec{n}$ is a source-frame (as opposed to rest-frame) vector. Define a source-frame unit vector $\vec{l}$ that points in the direction of the line-of-sight to the observer.

The element of the jet at $\vec{n}$ radiates isotropically in its own rest frame an amount of rest-frame energy per unit rest-frame solid angle

$$\frac{dE^{(R)}}{d^2\vec{l}^{(R)}}\, d^2\vec{n} = \frac{\gamma^{-1}E_\gamma^{(\rm T)}}{4\pi} \times \epsilon(\vec{n}\cdot\vec{b})\, d^2\vec{n}, \tag{20}$$

Here $\vec{l}^{(R)}$ is a unit direction vector pointing in the direction of the line-of-sight to the observer in the the rest frame of the jet element at $\vec{n}$. The profile function $\epsilon(\vec{n}\cdot\vec{b})$, which is azimuthally symmetric about the direction of the jet-axis unit vector $\vec{b}$, is normalized so that

$$\oint \epsilon(\vec{n} \cdot \vec{b})\, d^2\vec{n} = 2\pi \int_{-1}^{1} dx\, \epsilon(x) = 1. \tag{21}$$

The usual relativistic Doppler shift may be applied to yield the source-frame energy per unit source-frame solid angle:

$$\begin{aligned}
\frac{dE}{d^2\vec{l}} &= \oint \frac{dE^{(R)}}{d^2\vec{l}^{(R)}} \times \gamma^{-3}(1 - \beta\vec{n} \cdot \vec{l})^{-3}\, d^2\vec{n} \\
&= \frac{E_\gamma^{(T)}}{4\pi} \oint \epsilon(\vec{n} \cdot \vec{b}) \times \gamma^{-4}(1 - \beta\vec{n} \cdot \vec{l})^{-3}\, d^2\vec{n}.
\end{aligned} \tag{22}$$

Since this is an energy, rather than a luminosity, it should be converted to an observed fluence by means of a multiplication by $(1 + z)d_L(z)^{-2}$, where $d_L(z)$ is the usual luminosity distance.

The isotropic-equivalent energy is then given by

$$\begin{aligned}
E_{\text{iso}} &= 4\pi \times \frac{dE}{d^2\vec{l}} \\
&= E_\gamma^{(T)} \oint \epsilon(\vec{n} \cdot \vec{b}) \times \gamma^{-4}(1 - \beta\vec{n} \cdot \vec{l})^{-3}\, d^2\vec{n}.
\end{aligned} \tag{23}$$

We will also be interested in the inferred total energy, $E_\gamma^{(I)}$, which is given by

$$\begin{aligned}
E_\gamma^{(I)} &= 2\pi(1 - \cos\theta_{br}) \times \frac{dE}{d^2\vec{l}} \\
&= \frac{1}{2}(1 - \cos\theta_{br}) \times E_{\text{iso}},
\end{aligned} \tag{24}$$

where $\theta_{br} = \max(\theta_v, \theta_0)$, and θ_v is the viewing angle — the angular distance between the observer and the axis of the jet. Again, this assumes all the inferred energy is ascribed to a single jet lobe.

3.1.2.   Peak Energy

Another interesting calculation is the effective E_{peak} observed along the viewing direction, assuming a common rest-frame E_{peak} for the entire jet. For universal jet models, this

quantity can be placed in relation to $E_{\rm iso}$ and $E_\gamma^{\rm (I)}$, in order to examine whether the empirical $E_{\rm peak}$-$E_{\rm iso}$ relation of Amati et al. (2002), or the empirical $E_{\rm peak}$-$E_\gamma^{\rm (I)}$ relation of Ghirlanda et al. (2004) can be reproduced.

Technically, $E_{\rm peak}$ is the peak of the νF_ν spectrum obtained by superposing the appropriately Doppler-shifted and suitably Doppler-weighted spectra received from various parts of the jet. Performing this superposition explicitly presents difficulties, such as choosing a detailed shape of the underlying emission spectrum in such a way as to yield a Band (GRB) function (Band et al. 1993) spectrum for the superposition. This is the approach chosen by Yamazaki et al. (2002, 2003, 2004).

Our approach is to calculate the "photon-number averaged $E_{\rm peak}$." We ascribe a common rest-frame $E_{\rm peak}^{\rm (rest)}$ to the entire jet, and calculate the average Doppler-shifted $E_{\rm peak}$ in the viewing direction, where the average is weighted by photon number fluence. This is tantamount to computing the average of the Doppler shift $D \equiv \gamma^{-1}(1 - \beta\vec{n}\cdot\vec{l})^{-1}$, according to the weighting function $\epsilon(\vec{n}\cdot\vec{b}) \times \gamma^{-2}(1 - \beta\vec{n}\cdot\vec{l})^{-2}$ and applying it to the rest-frame $E_{\rm peak}$.

In other words, we want to be able to calculate

$$E_{\rm peak} = \langle D \rangle \times E_{\rm peak}^{\rm (rest)}, \tag{25}$$

where $E_{\rm peak}^{\rm (rest)}$ is the rest-frame peak energy, and

$$\langle D \rangle = \frac{\oint d^2\vec{n}\,\epsilon(\vec{n}\cdot\vec{b}) \times \gamma^{-3}(1 - \beta\vec{n}\cdot\vec{l})^{-3}}{\oint d^2\vec{n}\,\epsilon(\vec{n}\cdot\vec{b}) \times \gamma^{-2}(1 - \beta\vec{n}\cdot\vec{l})^{-2}}. \tag{26}$$

The accuracy of Eq. (25) as an estimator of the peak of the effective spectrum depends on the nature of the underlying rest-frame spectrum. In general, there will certainly be systematic uncertainties and biases in $\langle D \rangle E_{\rm peak}^{\rm (rest)}$ as an estimator of observed peak energy. Nonetheless, it seems reasonable to expect that in its functional dependence on θ_v, in its correlations with $E_{\rm iso}$ and $E_\gamma^{\rm (I)}$, and in its frequency distribution in universal jet models, the behavior of $\langle D \rangle E_{\rm peak}^{\rm (rest)}$ should not be too dissimilar from the behavior of the peak energy of the true composite spectrum. Since these are the properties that concern us, we adopt $\langle D \rangle$ as a proxy for $E_{\rm peak}$ in what follows.

One useful special case of $\langle D \rangle$ is $\epsilon(\vec{n}\cdot\vec{b}) = 1$ — isotropic outflow. In this case, it is straightforward to show that $\langle D \rangle = \gamma$. The reason this is useful is that this is also the limit to which $\langle D \rangle$ should tend when the profile ϵ varies weakly on angular scales comparable to γ^{-1} on the part of the jet that is moving parallel to the line-of-sight. It thus provides a valuable sanity check in practical computations.

3.1.3. Relativistic Corrections to Frequency Distributions of E_{iso} and $E_\gamma^{(I)}$.

It is interesting and important to understand the extent to which our §2 results on E_{iso} and $E_\gamma^{(I)}$ distributions of universal jet models are affected by relativistic corrections.

What is required is the form of dN/dE_{iso} and $dN/dE_\gamma^{(I)}$, where instead of being given directly in terms of the emission profile as we assumed above, E_{iso} and $E_\gamma^{(I)}$ are given by Eqs. (23) and (24).

Since in universal jet models the distribution of E_{iso} is entirely due to a uniform distribution in $\mu_v \equiv \cos\theta_v$, we may write

$$\frac{dN}{dE_{\text{iso}}} = \frac{dN/d\mu_v}{|dE_{\text{iso}}/d\mu_v|} = \frac{\text{const.}}{|dE_{\text{iso}}/d\mu_v|}. \tag{27}$$

We therefore need to calculate $dE_{\text{iso}}/d\mu_v$ starting from Eq. (23). This is accomplished by differentiating the Doppler factor in the integrand with respect to μ_v. By adopting spherical-polar coordinates (θ_v, ϕ_v) for $\vec{l}$ with the z-axis aligned with $\vec{b}$, and differentiating the quantity $\vec{n} \cdot \vec{l}$ with respect to μ_v while holding the ϕ_v and $\vec{n}$ fixed, it may be shown that

$$\frac{d(\vec{n} \cdot \vec{l})}{d\mu_v} = \frac{\vec{n} \cdot (\vec{b} - \mu_v \vec{l})}{1 - \mu_v^2}, \tag{28}$$

It follows then that if we differentiate Eq. (23) with respect to μ_v we obtain

$$\frac{dE_{\text{iso}}}{d\mu_v} = \frac{3\beta E_\gamma^{(\text{T})}}{\gamma^4(1 - \mu_v^2)} \oint d^2\vec{n} \, \frac{\epsilon(\vec{n} \cdot \vec{b})}{(1 - \beta\vec{n} \cdot \vec{l})^4}(\vec{n} \cdot \vec{b} - \mu_v \vec{n} \cdot \vec{l}). \tag{29}$$

We also require

$$\frac{dN}{dE_\gamma^{(I)}} = \frac{dN/d\mu_v}{|dE_\gamma^{(I)}/d\mu_v|} = \frac{\text{const.}}{|dE_\gamma^{(I)}/d\mu_v|}. \tag{30}$$

In Eq. (30) the factor $dE_\gamma^{(I)}/d\mu_v$ may be related to $dE_{\text{iso}}/d\mu_v$ using Eq. (24):

$$\frac{dE_\gamma^{(I)}}{d\mu_v} = \frac{1}{2}(1 - \mu_v)\frac{dE_{\text{iso}}}{d\mu_v} - \frac{1}{2}E_{\text{iso}}. \tag{31}$$

A special limiting case is the "needle" jet limit, where a narrow jet is observed off-axis (Yamazaki et al. 2002, 2003, 2004). In this case, $\epsilon(\vec{n} \cdot \vec{b})$ is so narrow that it acts as a δ-function. By Eq. (23), the radiation pattern is then proportional to $(1 - \beta\mu_v)^{-3}$. It is straightforward to show that in this limit, we have

$$\lim \frac{dN}{d\log E_{\text{iso}}} = E_{\text{iso}}^{-1/3}. \tag{32}$$

Furthermore, using Eq. (24), and using $\beta \approx 1$, we can also show that

$$\lim \frac{dN}{d\log E_\gamma^{(\mathrm{I})}} = E_\gamma^{(\mathrm{I})\,-1/2}. \tag{33}$$

These limits furnish useful sanity checks, and are interesting in their own right in the context of the off-axis beaming model (Yamazaki et al. 2002, 2003, 2004).

3.2. Spherical Convolution

We present in this section an efficient and general technique for computing the energy emission distributions of GRB jets with arbitrary (smooth) emission profiles.

3.2.1. Method

The quantities of interest described in the previous section are all expressed in terms of convolutions on the 2-sphere of two functions that are azimuthally symmetric but not mutually concentric. That is, they are of the form

$$\oint d^2\vec{n}\, f^{(1)}(\vec{n}\cdot\vec{q}^{(1)}) \times f^{(2)}(\vec{n}\cdot\vec{q}^{(2)}). \tag{34}$$

Now suppose we represent each of the two functions $f^{(1)}$ and $f^{(2)}$ on the two-sphere by their expansion in spherical harmonics. Since they are azimuthally symmetric, only the $m = 0$ spherical harmonics appear, that is

$$f^{(i)}(\vec{n}\cdot\vec{q}^{(i)}) = \sum_{l=0}^{\infty} f_l^{(i)} \frac{2l+1}{2} P_l(\vec{n}\cdot\vec{q}^{(i)}) \tag{35}$$

where the $P_l(x)$ are the usual Legendre polynomials, normalized so that $\int_{-1}^{1} P_l(x)^2\, dx = 2/(2l+1)$. By the orthogonality of the $P_l(x)$, it follows immediately that

$$f_l^{(i)} = \int_{-1}^{1} dx\, P_l(x) \times f^{(i)}(x). \tag{36}$$

If we let the z-direction be along $\vec{q}^{(1)}$ and define spherical polar coordinates (θ, ϕ) for $\vec{n}$, so that $\vec{n}\cdot\vec{q}^{(1)} = \cos\theta$, then in Eq. (35) we may replace $P_l(\vec{n}\cdot\vec{q}^{(1)})$ by $\sqrt{4\pi/(2l+1)}Y_l^0(\theta, \phi)$ in the expression for $f^{(1)}$.

If we introduce spherical polar coordinates (θ_2, ϕ_2) for the direction vector $\vec{q}^{(2)}$ (so that $\cos\theta_2 = \vec{q}^{(1)} \cdot \vec{q}^{(2)}$), we may also expand $P_l(\vec{n} \cdot \vec{q}^{(2)})$ in the expression for $f^{(2)}$ in Eq. (35), using the addition theorem of spherical harmonics:

$$P_l(\vec{n} \cdot \vec{q}^{(2)}) = \frac{4\pi}{2l+1} \sum_{m=-l}^{l} Y_l^m(\theta_2, \phi_2)\, Y_l^m(\theta, \phi)^*. \tag{37}$$

Substituting Eqs. (35) and (37) into Eq. (34), and using the orthogonality of spherical harmonics, we obtain

$$\oint d^2\vec{n}\, f^{(1)}(\vec{n} \cdot \vec{q}^{(1)}) \times f^{(2)}(\vec{n} \cdot \vec{q}^{(2)}) = \sum_{l=0}^{\infty} (2l+1)\, \pi\, P_l(\vec{q}^{(1)} \cdot \vec{q}^{(2)})\, f_l^{(1)}\, f_l^{(2)}. \tag{38}$$

Now, if either $f^{(1)}$ or $f^{(2)}$ is approximately band-limited to Legendre polynomials with $l < l_0$, then the sum in Eq. (38) is over a finite number of terms. We shall assume the approximate band-limitedness of the jet profile $\epsilon(\vec{n} \cdot \vec{b})$ in what follows. For jets characterized by an opening half-angle θ_0, the band limit l_0 will be in excess of π/θ_0.

The usefulness of Eq. (38) hinges upon our ability to calculate the *Legendre transform* integrals of Eq. (36), and to do so accurately and efficiently. We now consider how this is to be accomplished.

It is in principle possible to use the well-known recursion relations for the Legendre polynomials to obtain expressions for the higher-l transforms in terms of lower-l transforms, at least for the transforms of the Doppler factor and for the Fisher jet profile. Such a recursion scheme is unquestionably efficient. Unfortunately, it turns out to be inaccurate — the resulting recursion relations are unstable, and for physically interesting values of l_0 the transforms at the largest values of l can be dominated by amplified numerical noise.

The "Fast Legendre Transform" (FLT) algorithm of Driscoll & Healy (1994) is well-suited to our purposes. It is the spherical analogue of the celebrated FFT of Cooley & Tukey (1965), and has already become somewhat well-known in astrophysical circles, among analysts of CMB data (Oh, Spergel, & Hinshaw 1998; Wandelt & Gorski 2001)

Driscoll & Healy (1994) showed that for band-limited functions $f^{(i)}(x)$ with band limit l_0, the Legendre transform of Eq. (36) is exactly given by the quadrature formula

$$f_l^{(i)} = \sum_{j=0}^{2l_0-1} a_j^{(l_0)}\, f^{(i)}(\cos\theta_j)\, P_l(\cos\theta_j), \tag{39}$$

where

$$\theta_j \equiv \frac{\pi j}{2l_0} \tag{40}$$

$$a_j^{(l_0)} \equiv \frac{2}{l_0} \sin\left(\frac{\pi j}{2l_0}\right) \sum_{l=0}^{l_0-1} (2l+1)^{-1} \sin\left[\frac{(2l+1)\pi j}{2l_0}\right]. \tag{41}$$

In Eq. (41) we have corrected the normalization in the expression for the weights of Driscoll & Healy (1994), which was missing a factor $\sqrt{2}$.

Eq. (39) is the *Discrete Legendre Transform* (DLT), which is entirely analogous to the Discrete Fourier Transform. The band-limit l_0 plays a role analogous to that the Nyquist frequency – any power in the Legendre spectrum of $f^{(i)}(x)$ above l_0 is aliased by the DLT down to harmonics below l_0. For this reason, computation by means of spherical expansion is suitable for smooth jet profiles, such as the Fisher profile or the power-law profile. Profiles with sharp edges, such as the top-hat jet profile, can be expected to have substantial power at very high harmonics, and are therefore less well-suited to computation by this method. We will exhibit compact analytic emission formulas for the top-hat jet profile in §3.3 below.

Naive evaluation of the DLT evidently results in an expensive algorithm, one that is $\mathcal{O}(l_0{}^2)$. Physically interesting GRB jets are believed to be characterized by beaming angles $\gamma^{-1} \sim 10^{-2}$—10^{-3} radians, and by jet opening angles $\gtrsim 10^{-2}$ radians, implying values of l_0 in the several hundreds, or even above 1000. Particularly if many integrals are to be evaluated (as in a population-synthesis simulation, for example), the naive algorithm exacts a prohibitive cost.

Fortunately, Driscoll & Healy (1994) also exhibited the FLT: a fast — $\mathcal{O}(l_0 \log(l_0)^2)$ — algorithm modeled after the "Divide and Conquer" strategy of the FFT (Cooley & Tukey 1965). We have implemented this algorithm as a C library, and find it quite satisfactory for our present purposes. All computations of emission from Fisher and power-law profile jets exhibited in the next section were performed using this method.

3.2.2. Savings

In §3.1 we saw that the spherical convolutions in which we are interested combine $\epsilon(\vec{n} \cdot \vec{b})$ or $(\vec{n} \cdot \vec{b})\epsilon(\vec{n} \cdot \vec{b})$ with $(1 - \beta \vec{n} \cdot \vec{l})^{-n}$ ($n = 2, 3, 4$), or with $(\vec{n} \cdot \vec{l})(1 - \beta \vec{n} \cdot \vec{l})^{-4}$. A DLT (that is, a list of l_0 numbers) is required for each of the above convolvees. If each such DLT were computed as a separate FLT, the computational burden would rise to near-irritating levels.

Fortunately, it is not necessary to compute an FLT for each of these DLTs. The well-

known recursion relation $(2l + 1)xP_l(x) = (l + 1)P_{l+1}(x) + lP_{l-1}(x)$ among the Legendre Polynomials, together with the relation $(1 - \beta x)^{-n+1} = (1 - \beta x) \times (1 - \beta x)^{-n}$ allow us to relate the DLT of $(1-\beta x)^{-n}$ ($n = 2, 3$), and the DLT of $x(1-\beta x)^{-4}$ to the DLT of $(1-\beta x)^{-4}$, and also to relate the DLT of $x \times \epsilon(x)$ to the DLT of $\epsilon(x)$.

It is thus only necessary, for the purposes of the present work, to calculate the DLTs of $\epsilon(x)$ and of $(1 - \beta x)^{-4}$. The other DLTs are then computable essentially for free. If it were not of interest to calculate the distributions of §3.1.3, it would only be necessary to compute the DLTs of $\epsilon(x)$ and of $(1 - \beta x)^{-3}$, in order to compute E_{iso} and E_{peak}.

Note also that since the two required DLTs are independent of the viewing angle θ_v, the processing expense of calculating those DLTs is incurred once, after which the stored DLTs may be reused for many values of the viewing angle θ_v.

3.2.3. Numerical Limitations

Eq. (38) has the form of an inner product with a weighting function proportional to $P_l(\vec{q}^{(1)} \cdot \vec{q}^{(2)})$. In the cases we consider here, the argument of the Legendre polynomial is the cosine of the viewing angle, $\cos \theta_v$. When θ_v is close to zero, the Legendre polynomial is nearly 1, and the terms in the inner product add constructively. This behavior is necessary so that maximum emission is obtained when the observing direction is aligned with the jet axis.

As the observing direction moves away from the jet axis, terms in the inner product must begin to engage in some mutual cancellation, in order to produce the expected decrease in fluence. If the underlying profile spans many orders of magnitude (as the Fisher profile may easily do), then it may come to pass that the cancellations required to produce the necessary suppression of fluence at large θ_v cannot occur in practical computations, as they are drowned out by numerical noise due to the finite machine precision.

The most commonly encountered form of floating-point double precision is constructed from 8-byte words, which afford a relative spacing between adjacent representable floating point numbers of about 10^{-14}. This is the smallest relative magnitude that can be attained, using such arithmetic, in calculations that depend on delicate cancellation.

If we demand a minimum accuracy of 1%, we may therefore expect that the computable dynamic range of E_{iso} (say) is no more than about 12 decades, using 8-byte reals. This expectation is in fact borne out by experience. Of course this is plenty of dynamic range for the present purposes. Should greater dynamic range be nonetheless required, some additional

decades may be secured by adopting extended precision (typically 16-byte floating point words), and possibly computing with machine architectures endowed with a larger natural word size.

3.2.4. "Smooth" Power-Law Profiles

Power-law profiles diverge at the jet axis. It is customary to deal with this deplorable behavior by truncating the power-law at some small angle (Zhang & Mészáros 2002). This practice represents a problem for our spherical-expansion approach, since the sharp edge at the cutoff injects unwanted spectral power into the DLT of ϵ_{PL} at high values of l.

Consequently, the normalized power-law profile that we actually use in this work is

$$\epsilon_{\mathrm{PL}}(\cos\theta) = \kappa(1 - \cos\theta + {\theta_0}^2/2)^{-\delta}, \tag{42}$$

where we have introduced a smooth cut-off θ_0, rather than truncate the power-law. The resulting profile has a smooth, cusp-free peak in θ at $\theta = 0$.

The (single-lobe) normalization factor κ is given by

$$\kappa = \begin{cases} \frac{1-\delta}{2\pi\left[(2+{\theta_0}^2/2)^{1-\delta} - ({\theta_0}^2/2)^{1-\delta}\right]} & : \quad \delta \neq 1 \\[2ex] \frac{1}{2\pi\log(4{\theta_0}^{-2}+1)} & : \quad \delta = 1 \end{cases} \tag{43}$$

The effective angular width of this profile is a function of both θ_0 and δ. A simple estimator of this width may be constructed by making a Gaussian approximation to the jet near the peak. The width of this Gaussian is then approximately

$$\begin{aligned} \theta_w &\equiv \left|\frac{d^2\log\epsilon_{\mathrm{PL}}}{d\theta^2}\right|^{-1/2} \\ &= \theta_0/\sqrt{2\delta}. \end{aligned} \tag{44}$$

Thus for a reasonable range of δ near $\delta = 1$, θ_0 is itself not a bad estimator of the jet width. For large δ, however, it is advisable to regard θ_w, rather than θ_0, as the effective angular width of the profile.

In particular, when we calculate $E_\gamma^{(\mathrm{I})} = E_{\mathrm{iso}} \times (1 - \cos\theta_{br})$ for power-law profiles, we always use a break angle $\theta_{br} = \max(\theta_v, \theta_w)$, rather than the "naive" prescription $\theta = \max(\theta_v, \theta_0)$.

3.2.5. Emission From Afterglow Jets

The main focus of the current work is prompt GRB emission, so we are not really concerned with afterglow emission. Nonetheless, it is worthwhile to digress briefly on the applicability of our spherical convolution strategy to afterglows.

In prompt emission, it is quite reasonable to assume that γ is constant throughout the duration of the burst (Rees & Mészáros 1994). This assumption underlies our expressions for the various emission formulas derived above.

Afterglow emission is another story. The external shock model features a deceleration of the shock front, due to interaction with the ISM (Piran 1999). This means that photons received simultaneously by the observer from different parts of the shock front were actually emitted at epochs characterized by different values of γ — there is a relativistic "look-back" effect that must be taken properly into account (Woods & Loeb 1999; Granot et al. 1999). It may seem that this effect compromises the usefulness of the methods introduced in this section, by making the main emission formulas take forms that cannot be cast as convolutions on the 2-sphere.

In fact, subject to the assumption that the *shape* of the underlying emission profile is invariant (so that only the emission amplitude varies with time), it is still possible to write the emission formulas as 2-sphere convolutions, so that the present approach using decompositions in Legendre polynomials may still be valuable for afterglow studies.

This is the case because at each observer time t_o, a photon received from the element of the jet at $\vec{n}$ was emitted at a time $t(t_o, \vec{n} \cdot \vec{l})$ that is a function of $\vec{n} \cdot \vec{l}$, where $\vec{l}$ is the viewing direction. This function is computable in terms of the jet velocity history, $\beta(t)$. If the jet emission profile (now a function of time) has by assumption the form

$$E(t, \vec{n}) = A(t)\epsilon(\vec{n} \cdot \vec{b}), \tag{45}$$

then the instantaneous flux is proportional to a convolution like that of Eq. (34), where

$$f^{(1)}(\vec{n} \cdot \vec{b}) = \epsilon(\vec{n} \cdot \vec{b}), \tag{46}$$

$$f^{(2)}(\vec{n} \cdot \vec{l}) = A\left(t(t_o, \vec{n} \cdot \vec{l})\right) \times \left[1 - \beta\left(t(t_o, \vec{n} \cdot \vec{l})\right)\vec{n} \cdot \vec{l}\right]^{-3}. \tag{47}$$

It follows that under a moderately restrictive assumption about the time development of the emission profile, afterglow emission may also be treated by decomposition into Legendre polynomials, as described above. A possible generalization of this approach that relaxes the above restriction somewhat is to consider profiles constituted of linear superpositions of terms like the one in Eq. (45).

Note another assumption made here, however: we still require that γ is uniform across the jet. In fact, afterglow jet models with spatial variation in γ are considered in the literature (Rossi et al. 2002; Granot & Kumar 2003). If the uniform-γ assumption is removed, the required factorization of the integrand into $f^{(1)}(\vec{n} \cdot \vec{b})$ and $f^{(2)}(\vec{n} \cdot \vec{l})$ fails, and direct expansion in Legendre polynomials is no longer an available strategy. If the variation of γ across the jet is not too strong, however, it is still possible to adopt the spherical expansion method after expanding the Doppler factor in powers of the deviation of γ from its value on the jet axis, $\gamma(\vec{n}) - \gamma(\vec{b})$.

3.3. Emission From Top-Hat Jet Profiles

As mentioned above, the sharp edge of a top-hat jet profile forces unwanted power onto the higher harmonics of its DLT. Fortunately, there are closed-form analytical expressions for the emission from a top-hat jet profile, which we present here.

3.3.1. Emission Formulas

The emission profile of a top-hat jet of opening half-angle θ_0 is

$$\epsilon_{TH}(\cos\theta) = [2\pi(1 - \cos\theta_0)]^{-1}\,\Theta(\cos\theta - \cos\theta_0), \qquad (48)$$

where $\Theta(x)$ is the Heaviside step function. From Eq. (23) we then have

$$
\begin{aligned}
E_{\text{iso}} &= \frac{E_\gamma^{(\text{T})}}{2\pi\gamma^4(1 - \cos\theta_0)} \oint d^2\vec{n}\, \frac{\Theta(\vec{n} \cdot \vec{b} - \cos\theta_0)}{(1 - \beta\vec{n} \cdot \vec{l})^3} \\
&= \frac{E_\gamma^{(\text{T})}}{2\pi\gamma^4(1 - \cos\theta_0)} \int_{\cos\theta_0}^{1} d\cos\theta \int_{-\pi}^{\pi} \frac{d\phi}{[1 - \beta(\cos\theta_v \cos\theta + \sin\theta_v \sin\theta \cos\phi)]^3}, \quad (49)
\end{aligned}
$$

where again θ_v is the angle between $\vec{b}$ and $\vec{l}$.

The integral over ϕ may be performed using formula 3.661.4 of Gradshteyn & Rhyzik (1965, p.383). The remaining integral over $\cos\theta$ may then be performed by means of the successive substitutions $y = \beta\cos\theta - \cos\theta_v$, $\tan q = \gamma y/\sin\theta_v$. The result is

$$E_{\text{iso}} = \frac{E_\gamma^{(\text{T})}}{2\beta\gamma^4(1 - \cos\theta_0)} \left[f(\beta - \cos\theta_v) - f(\beta\cos\theta_0 - \cos\theta_v) \right], \qquad (50)$$

where

$$f(z) \equiv \frac{\gamma^2(2\gamma^2 - 1)z^3 + (3\gamma^2\sin^2\theta_v - 1)z + 2\cos\theta_v \sin^2\theta_v}{(z^2 + \gamma^{-2}\sin^2\theta_v)^{3/2}}. \qquad (51)$$

From Eq. (26), the average Doppler factor $\langle D \rangle$ is expressed as a ratio of two integrals, one of which is the same as the one in Eq.(49), while the other is quite similar and may be calculated using the same technique. The result is

$$\langle D \rangle = \gamma^{-1} \frac{f(\beta - \cos\theta_v) - f(\beta\cos\theta_0 - \cos\theta_v)}{g(\beta - \cos\theta_v) - g(\beta\cos\theta_0 - \cos\theta_v)}, \tag{52}$$

where $f(z)$ is as in Eq. (51), while the function $g(z)$ is given by

$$g(z) \equiv \frac{2\gamma^2 z + 2\cos\theta_v}{(z^2 + \gamma^{-2}\sin^2\theta_v)^{1/2}}. \tag{53}$$

The frequency distribution of $E_{\rm iso}$ is generally given by Eq. (27). This formula may be applied with Eq. (50) to yield an expression for $dN/dE_{\rm iso}$ that is suitable for computation. This expression is algebraically obvious, but burdensome, and will be omitted here.

4. Jet Profiles And Their Signatures

We now turn directly to the observable signatures of universal jet models based on Fisher, power-law, and top-hat jet profiles.

Our approach is to explore the parameter space of universal jet models based on these families of profiles, assessing features of the landscape for their resemblance or dissimilarity to the empirically-known properties of GRBs discussed earlier. We do not intend here to make quantitative judgments of how well the models "fit" the data. Rather, we wish to construct a map of the parameter space of universal-jet GRB models, so as to clarify the strengths and weaknesses of each profile choice. This allows one to choose which aspects of the data can be modeled successfully using a particular family of universal-jet models, and which must be "evaded" by invoking new model features. It also allows easier interpretation of the results of population-synthesis simulations that attempt to reproduce the distributional and correlational properties of $E_{\rm iso}$, $E_\gamma^{(\rm I)}$, and $E_{\rm peak}$, irrespective of whether the models adopted are of the universal or variable-geometry variety.

This map is also a useful tool with respect to models that make more realistic observable choices than ours. Our variables are admittedly simplistic, insofar as comparison with data from real GRB detectors are concerned. $E_{\rm iso}$ is a bolometric quantity, which makes no reference to detector bandpass, and $\langle D \rangle \times E_{\rm peak}^{(\rm rest)}$ is a somewhat crude representation of the true spectral peak. More realistic modeling ascribes an actual rest-frame spectrum to the jet, possibly even allowing for spectral variation over the surface of the shock. Even more

realistic would be the introduction of time variability, so as to allow more detailed modeling of detector thresholds.

What such modeling gains in fidelity, however, it loses in performance. It is an extremely burdensome task to compute emission, correlation, and distributional properties from models that must integrate numerically across the shock surface, the photon frequency domain, and the time domain. Such investigations cannot currently be carried out over wide swaths of parameter space. This is where our map can be valuable, by indicating qualitatively the kinds of models and relatively narrow ranges of parameters that are worth a closer look, and where builders of complicated models might consider unlimbering their heavy machinery.

In this section we consider the following families of universal GRB jet models:

- Fisher profile universal jets

- Power-law profile universal jets, with power-law indices δ=1, 2, and 8.

- Top-hat profile universal jets.

For each family of models, we exhibit six kinds of plots: $E_{\rm iso}$ versus θ_v, $\langle D \rangle$ versus θ_v, $E_{\rm iso}$ versus $\langle D \rangle$ ("Amati" plot), $E_\gamma^{(I)}$ versus $\langle D \rangle$ ("Ghirlanda" plot), $dN/d \log E_{\rm iso}$ frequency plot, and $dN/d \log E_\gamma^{(I)}$ frequency plot.

In each case we allow γ to take the values 10, 33.3, 100, and 333.

Each family of profiles has a parameter θ_0, which characterizes the angular width of the profile. Its interpretation is specific to the functional form of the profile. In almost all cases, we allow θ_0 to take the values 0.1, 0.3, 0.01, and 0.003. The one exception is the power-law profile with $\delta = 8$. In this case we actually select $\theta_0 = 0.4$, 0.12, 0.04, and 0.012, so as to make the effective width estimator θ_w of Eq. (44) take the values θ_w =0.1, 0.3, 0.01, and 0.003.

The region of parameter space covered by these choices of parameter values includes a subregion where γ^{-1} is larger than the characteristic width of the underlying jet profile (θ_0 or θ_w, as the case may be). This subregion of parameter space may be considered unphysical on hydrodynamic grounds (Rhoads 1999; Sari et al. 1999), since a hydrodynamic jet expands sideways rather than expanding ballistically with a constant shape in this regime. Furthermore, general arguments of hydrodynamic causality during the acceleration phase suggest that the angular scale of the jet should be quite comparable to γ^{-1} (Stern 2003, Lazzati 2005, private communication). On the other hand, there is evidence that MHD jets can sustain degrees of collimation that easily violate this constraint (Lapenta & Kronberg

2005). We do not intend to discuss the details of these physical pictures here. We simply consider this region in our study for the sake of completeness.

4.1. Emission From Fisher Jet Profiles

In what follows, we use the single-lobe normalized Fisher jet profile:

$$\epsilon_{\text{Fisher}}(\cos\theta) = \frac{e^{\cos\theta/{\theta_0}^2}}{4\pi{\theta_0}^2\sinh{\theta_0}^{-2}}. \tag{54}$$

4.1.1. Emission

The four panels of Fig. 3 show the behavior of E_{iso} as a function of viewing angle θ_v. The noteworthy feature of these plots is that the value of γ^{-1} sets a lower limit to the effective angular size of the emission pattern. The characteristic angular width of radiation patterns from jets with $\theta_0 < \gamma^{-1}$ is set by γ^{-1}, not θ_0, since in this limit the jet effectively resembles "needle jet," whose emission pattern is essentially set by the Doppler function. This effect is particularly conspicuous in the lower-right hand panel of Fig. 3, in which the intrinsic profile width is 0.003 radians, while all of the emission patterns are in fact considerably broader than this.

This jet-broadening effect is a ubiquitous feature of relativistic kinematics, that recurs in all the other profiles as well.

The four panels of Fig. 4 show the behavior of $\langle D \rangle$ as a function of viewing angle θ_v. Here a curious feature requires explanation: there is a "shelf" that appears in the $\langle D \rangle$ function near the jet axis, which for large γ extends considerably beyond the value of θ_0. For $\theta_0 = 0.1$, the $\gamma = 333$ curve has a shelf that extends out to $\theta_v = 0.5$, taking up about 12% of a hemisphere.

The explanation of the shelf is seen in the four panels of Fig. 5. These plots show the photon "provenance" distribution for an observer viewing a Fisher jet with parameters $\gamma = 333$, $\theta_0 = 0.1$, at viewing angle θ_v. The curve in each panel is a slice through the plane containing $\vec{l}$ and $\vec{b}$ of the function $\epsilon_{\text{Fisher}}(\vec{b}\cdot\vec{n}) \times (1 - \beta\vec{l}\cdot\vec{n})^{-2}$, plotted as a function of angle θ from $\vec{b}$. Ignoring the azimuthal direction for the sake of simplicity, this is the (un-normalized) probability that a photon directed along $\vec{l}$ should have been emitted from a location on the shock surface that is at an angle θ from the jet axis. The four panels show this curve for four different viewing angles — $\theta_v = 0.2$, 0.45, 0.6, and 0.75. The corresponding point on the

corresponding $\langle D \rangle - \theta_v$ plot of Fig. 4 is shown in the inset. Angular scales are represented linearly in these plots, the better to bring out the detail.

The dashed line shows the position of the "Doppler-mean" viewing angle $\langle \theta \rangle$ — that is the angle such that $\gamma^{-1}[1 - \beta \cos(\theta_v - \langle \theta \rangle)]^{-1} = \langle D \rangle$. It represents the provenance of the photons most responsible for giving $\langle D \rangle$ its current value.

It can be seen from these plots that $\langle \theta \rangle$ is simply tracking the mass of the distribution, whose location and extent is determined by the interplay between the Fisher function and the Doppler photon distribution. Near the axis of the jet, the peak of the Doppler factor dominates, and almost all the received photons originate from locations on the jet that are moving towards the observer (top left panel).

When the viewing angle gets large enough, the Doppler peak starts to peel away from the jet axis. The provenance distribution begins to develop a bimodal character (with the Doppler mode still dominant), so the mean photon provenance shifts slightly away from the part of the jet moving towards the observer, towards the axis of the jet. This is the beginning of the shelf drop-off (top right panel).

As the viewing angle continues to grow, the jet axis peak of the distribution becomes more and more competitive with the Doppler peak, pulling $\langle \theta \rangle$ substantially away from the part of the jet moving towards the observer (bottom left panel).

Finally, at large viewing angles, the Doppler peak is eclipsed by the jet axis peak. The value of $\langle \theta \rangle$ approaches θ_0, and changes very little thereafter. From here on out, the jet appears to the observer as a needle, with no angular structure as far as $\langle D \rangle$ is concerned (bottom right panel).

The presence of this shelf at the bright end of universal Fisher jet models with $\gamma^{-1} \ll \theta_0$ is potentially very constraining on such models. We have already noted that in the case of $\gamma = 333$, $\theta_0 = 0.1$, the shelf takes up 12% of a hemisphere. In the context of a universal model, this means that for these parameters, the brightest 12% of GRBs should belong to a sub-population with constant $\langle D \rangle$ and hence with constant E_{peak}. Such a concentration might very well be conspicuous. As we will see, it also strongly distorts the $E_{\mathrm{iso}}-\langle D \rangle$ and $E_\gamma^{(I)}-\langle D \rangle$ relations away from their empirical forms.

4.1.2. $E_{iso} - \langle D \rangle$ and $E_\gamma^{(I)} - \langle D \rangle$ Correlations

The four panels of Fig. 6 show the behavior of the $E_{\mathrm{iso}}-\langle D \rangle$ ("Amati") correlation in universal Fisher models with our standard parameter choices. The axis scales are chosen

so that a slope of 0.5 appears as a 45° line, in order to ease the search for an "Amati-like" slope.

The 1/3 slope characteristic of off-axis emission from "needle" jets is seen to hold for $\theta_0 \ll \gamma^{-1}$. This part of parameter space is unpromising, since the empirical slope is known to be 0.5 (Amati et al. 2002; Lamb et al. 2004).

For $\gamma^{-1} \ll \theta_0$, there does appear a section of the $E_{\rm iso}$–$\langle D \rangle$ curve that seems to have the empirically-observed slope. This part of the curve does not, however, include the brightest — and most easily observable — events. In fact, the "Amati-like" part of the curve corresponds to the narrow "cliff" of Fig. 4. For $\gamma = 333$, $\theta_0 = 0.1$ (lower left panel), for example, it comprises only viewing angles θ_v between 0.5 and 0.7, subtending only 11% of a hemisphere, compared to the 12% subtended by the shelf. The case of $\gamma = 333$, $\theta_0 = 0.03$ (upper right panel) seems more promising, since now the shelf sets in at about $\theta_v = 0.1$, subtending a much smaller solid angle.

It appears, then, that a fit of a universal Fisher jet to "Amati"-type data could be extremely constraining on the model parameters. The necessity of producing the Amati slope, while at the same time not inflicting on the model predictions a sub-population of events from the shelf with zero slope that is brighter than, and comparably numerous to, the "Amati-like" sub-population, would in all likelihood result in a narrow acceptable region of γ-θ_0 parameter space.

The four panels of Fig. 7 show the behavior of the $E_\gamma^{(\rm I)}$–$\langle D \rangle$ ("Ghirlanda") correlation in universal Fisher models with our standard parameter choices.

The $\theta_0 < \gamma^{-1}$ limit appears to feature a slope of 0.5, as opposed to the empirically-determined value of 0.7 (Ghirlanda et al. 2004), so again this part of parameter space is not promising territory for this family of models.

For $\gamma^{-1} \ll \theta_0$, there is a steeper slope, corresponding again to the drop-off from the shelf (as may be determined by comparison with Fig. 4). For $\theta_0 = 0.1$, $\gamma = 333$ (upper left panel), this slope is 1. It drops down to zero at high values of $E_\gamma^{(\rm I)}$. Similar behavior is seen for $\theta_0 = 0.03$, $\gamma = 333$ (upper right panel). The difference between the two curves is that the flattening-out takes place over a narrower range in θ_v when $\theta_0 = 0.03$ than when $\theta_0 = 0.1$, reducing the anomalous zero-slope sub-population. So just as for the Amati case, it appears that a fit of a universal Fisher jet to "Ghirlanda"-type data could produce very strict constraints on γ and θ_0.

One feature of Fig. 7 requiring an explanation is the hook-like structure observed for $\gamma^{-1} > \theta_0$, in which $E_\gamma^{(\rm I)}$ appears to fold back upon itself.

This feature is another side-effect of the jet-broadening effect noted above. The relativistic kinematics is cutting off the jet profile when $\theta_v \sim \gamma^{-1}$, long before θ_v approaches θ_0. Therefore, the factor $1 - \mu_v$ in the definition of $E_\gamma^{(\mathrm{I})}$ (Eq. 10) begins to depress the value of $E_\gamma^{(\mathrm{I})}$ earlier and more deeply than it could the "bare" fisher profile. With reference to the schematic Fig. 2, the maximum of the curve is occurring at lower values of μ_v, and the curve plunges to much lower values before it "recovers" at $\theta_v = \theta_0$.

What this indicates is that when relativistic kinematics are taken into account, it would be best to apply the Frail et al. (2001) procedure using a break angle $\theta_{br} = \max(\theta_v, \theta_0, \gamma^{-1})$, in order to avoid such artifacts.

4.1.3. E_{iso} and $E_\gamma^{(I)}$ Frequency Distributions

The four panels of Fig. 8 show the effect of relativistic kinematics on the uniform E_{iso} frequency distributions of universal Fisher jets that were derived in §2.1. In each panel, the light solid line shows the "bare" value of the distribution, corresponding to the (uniform) shape derived just from the profile. Essentially, this is the $\gamma \to \infty$ limit.

We see here that with $\gamma^{-1} \ll \theta_0$, the uniform distribution that was built into the Fisher profile by construction is largely preserved for bright events. As θ_0 decreases, the jet emission behaves more and more like off-axis emission from a needle jet, which by Eq. (32) is a power-law with a slope of -1/3. Accordingly, the frequency distributions depart more and more from the uniform shape that was due to the Fisher profile.

The four panels of Fig. 9 show the effect of relativistic kinematics on the broad $E_\gamma^{(\mathrm{I})}$ distributions of universal Fisher jets that were derived in §2.1. The "bare" distribution is again shown by the light solid line. Just as for the E_{iso} frequency plots, these distributions remain broad, in resemblance to the "bare" version, until θ_0 becomes so small that the emission is characteristic of an off-axis needle jet, at which point they assume the shape of a power-law with a slope of -1/2, as expected from Eq. (33).

4.2. $\delta = 1$ Power-Law Jet Profiles

4.2.1. Emission

The four panels of Fig. 10 show the behavior of E_{iso} as a function of viewing angle θ_v for the power-law profile with index $\delta = 1$. Once again, we see the "jet-broadening" effect, in which the effective angular size of the jet radiation pattern is set by whichever is larger of θ_0

and γ^{-1}. These radiation patterns have broad tails in every case, reflecting the fact that this profile falls off more gradually than the Doppler photon distribution function $\gamma^{-2}(1 - \beta\mu)^{-2}$.

The four panels of Fig. 11 show the behavior of $\langle D \rangle$ as a function of viewing angle θ_v. The striking feature of these plots is the extremely restricted dynamic range of $\langle D \rangle$.

The large-θ_v limit in each case is $\langle D \rangle = \gamma$, as is expected by the fact that far from the jet axis, this profile falls so gradually that it looks nearly uniform (recall from §3.1.2 that γ is the "uniform outflow" limit of $\langle D \rangle$). This reason for this large-θ_v limit of $\langle D \rangle$ also helps explain why the dynamic range of $\langle D \rangle$ is so limited — this profile varies quite gently almost everywhere, so its $\langle D \rangle$ deviates only moderately from γ almost everywhere. The only real chance that $\langle D \rangle$ has to run away is near $\theta_v = 0$, but even here it is eventually reined in by the cutoff. The smaller θ_0, the wider the available range of $\langle D \rangle$, but it is clear that uncomfortably small values of θ_0 will be required in order to allow this profile to produce the kind of range of E_{peak} — at least two orders of magnitude — that is observed in GRBs.

4.2.2. $E_{iso} - \langle D \rangle$ and $E_\gamma^{(I)} - \langle D \rangle$ Correlations

The four panels of Fig. 12 show the behavior of the E_{iso}–$\langle D \rangle$ ("Amati") correlation in universal $\delta = 1$ power-law models with our standard parameter choices.

Here we see the some of the trouble created by the limited dynamical range of $\langle D \rangle$. The curves stay more-or-less flat for much of the dynamical range of E_{iso}. The high-γ curves do suddenly rear up at high E_{iso}, but not nearly enough to make a convincing Amati plot, and in any event, comparison with Figs. 11 and 10 show that this is going on over a very small region of θ_v, corresponding to a tiny fraction of observed bursts in a universal jet model.

The four panels of Fig. 13 show the behavior of the $E_\gamma^{(I)}$–$\langle D \rangle$ ("Ghirlanda") correlation in universal $\delta = 1$ power-law models with our standard parameter choices.

There seems to be no hope for a real "Ghirlanda" relation with this profile. Due to the limited dynamic range of $\langle D \rangle$, the trajectory is essentially flat, with a hook-like structure at the very end due to the same side-effect of relativistic jet-broadening that was remarked upon in §4.1.2.

4.2.3. E_{iso} and $E_\gamma^{(I)}$ Frequency Distributions

The four panels of Fig. 14 show the effect of relativistic kinematics on the E_{iso} frequency distribution of $\delta = 1$ power-law jets — see Eq. (18). Again, the "bare" ($\gamma \to \infty$) distribution

is shown by a light solid line, whose slope in this case is -1.

We see here that the distribution of dN/dE_{iso} appears to be irreducibly narrow, and relativistic kinematics are powerless to broaden it. From this it appears that this "extremal" power-law profile cannot under any circumstances reproduce the broad — and very nearly uniform in $\log E_{\text{iso}}$ — distribution that is observed empirically in GRBs.

The four panels of Fig. 15 show the relativistic broadening of the δ-function distribution designed into this profile — see Eq. (19). It clearly succeeds in preserving its empirically-desirable narrowness.

4.3. $\delta = 2$ **Power-Law Jet Profiles**

The results of §4.2 are to some extent anomalous for power-law jets, since $\delta = 1$ is a singular case as far as $E_\gamma^{(\text{I})}$ is concerned. The $\delta = 2$ case comprises more typical behavior.

4.3.1.   Emission

The four panels of Fig. 16 show the behavior of E_{iso} as a function of viewing angle θ_v for a power-law profile with $\delta = 2$. We see jet broadening again, as expected. The tails at high θ_v are no longer independent of γ, as they were for $\delta = 1$, since now the profile function falls off as rapidly as the Doppler photon distribution function. The available dynamic range of E_{iso} is thereby increased.

The four panels of Fig. 17 show the behavior of $\langle D \rangle$ as a function of viewing angle θ_v. We see that $\langle D \rangle$ can now just about produce two orders of magnitude's worth of dynamic range, in the "needle jet" approximation ($\theta_0 \ll \gamma^{-1}$), but the dynamic range again becomes quite restricted in other regimes. For $\theta_0 > \gamma^{-1}$, the large-θ_v limit of $\langle D \rangle$ is still γ, as expected, and this limit still serves to constrain the available range of $\langle D \rangle$.

4.3.2. E_{iso} – $\langle D \rangle$ and $E_\gamma^{(I)}$ – $\langle D \rangle$ Correlations

The four panels of Fig. 18 show the behavior of the E_{iso}–$\langle D \rangle$ ("Amati") correlation in universal $\delta = 2$ power-law models with our standard parameter choices.

Here it appears that this profile is trapped between a rock and a hard place. In order to make enough dynamic range in $\langle D \rangle$, it must enter the "needle jet" regime ($\theta_0 \ll \gamma^{-1}$). But

as soon as it does so, the slope of the $E_{\rm iso}$–$\langle D \rangle$ curve becomes 1/3, as expected for off-axis emission from narrow jets. It does not appear that this profile can make an "Amati" relation spanning two decades of $E_{\rm peak}$.

The four panels of Fig. 19 show the behavior of the $E_\gamma^{(\rm I)}$–$\langle D \rangle$ ("Ghirlanda") correlation in universal $\delta = 2$ power-law models with our standard parameter choices.

We can see from these curves that this profile's ability to make a respectable "Ghirlanda" relation is no better than it's ability to make "Amati" relations, and for the same reasons.

4.3.3. E_{iso} and $E_\gamma^{(I)}$ Frequency Distributions

The four panels of Fig. 20 show the effect of relativistic kinematics on the $E_{\rm iso}$ frequency distribution of $\delta = 2$ power-law jets — see Eq. (18). Again, the "bare" ($\gamma \to \infty$) distribution is shown by a light solid line, whose slope in this case is -1/2.

The distribution of $dN/dE_{\rm iso}$ is still narrower than the data seem to indicate, although in the "needle-jet" limit $\theta_0 \ll \gamma^{-1}$, the slope of the distribution is softened by relativistic kinematics to the -1/3 index power-law expected from Eq. (32).

The four panels of Fig. 21 show the effect of relativistic kinematics on the $E_\gamma^{(\rm I)}$ frequency distribution of power-law jets — see Eq. (19). The distribution can easily be made acceptably narrow, although in the "needle-jet" limit $\theta_0 \ll \gamma^{-1}$, the -1/2 slope expected from Eq. (33) seems somewhat less steep than is consistent with the data. This means that a fit of such a universal model could potentially provide a (model-dependent) lower limit on γ.

4.4. $\delta = 8$ Power-Law Jet Profiles

The chief difficulty encountered by the relatively shallow $\delta = 2$ index power-law of §4.3 is a lack of dynamic range, particularly for $\langle D \rangle$. It is therefore interesting to examine whether this weakness can be addressed by adopting a steeper power-law index. Here we examine $\delta = 8$. As a reminder, our standard parameter values are altered here, to $\theta_0 = 0.4$, 0.12, 0.04, and 0.012, so as to make the effective width estimator θ_w of Eq. (44) take the values $\theta_w = 0.1$, 0.3, 0.01, and 0.003.

4.4.1. Emission

The four panels of Fig. 22 show the behavior of $E_{\rm iso}$ as a function of viewing angle θ_v for a power-law profile with $\delta = 8$. We see jet broadening again, as expected. For larger values of γ, this profile appears to be able to produce a fairly wide variety of radiation patterns, and great dynamic range of $E_{\rm iso}$.

The four panels of Fig. 23 show the behavior of $\langle D \rangle$ as a function of viewing angle θ_v. Here we can finally see strong dynamic range of $\langle D \rangle$ in a power-law model, at least for narrow jets. We also see the return of the "shelf" feature that was noted in §4.1.1, which appears to be a generic feature of steep profiles.

4.4.2. E_{iso} – $\langle D \rangle$ and $E_\gamma^{(I)}$ – $\langle D \rangle$ Correlations

The four panels of Fig. 24 show the behavior of the $E_{\rm iso}$–$\langle D \rangle$ ("Amati") correlation in universal $\delta = 8$ power-law models. The axis scales are chosen so that a slope of 0.5 appears as a 45° line, in order to ease the search for an "Amati-like" slope.

Here it appears that slopes steeper than $1/3$ can be produced, possibly even over a sufficiently large dynamic range of $E_{\rm iso}$ and $\langle D \rangle$, at the cost of some flattening out near the bright end of the distribution. The slope of the $\theta_0 = 0.04$, $\gamma^{-1} = 0.003$ curve (bottom left panel), for example, is about 0.68 at intermediate $E_{\rm iso}$, and by comparison with Fig. 23 (bottom right panel), the flattening out at high values of $\langle D \rangle$ only sets in at about $\theta_v = 0.1$, subtending only 5×10^{-3} of a hemisphere. While the slope is high compared to the standard Amati value of 0.5, it appears possible that there could be a value of δ bracketed between $\delta = 2$ and $\delta = 8$ that can reproduce the Amati slope.

The four panels of Fig. 25 show the behavior of the $E_\gamma^{(I)}$–$\langle D \rangle$ ("Ghirlanda") correlation in universal $\delta = 8$ power-law models.

Just as for the "Amati" correlation plots, there appears to be a range of parameter space with relatively steep slope and large dynamic range of $\langle D \rangle$. The slope of the $\theta_0 = 0.04$, $\gamma^{-1} = 0.003$ curve (bottom left panel), for example, is about 0.83 at intermediate $E_{\rm iso}$, and again the flattening at high energy subtends a tiny solid angle. It thus appears possible that there could be a value of δ bracketed between $\delta = 2$ and $\delta = 8$ that can reproduce the Ghirlanda slope.

4.4.3. E_{iso} and $E_\gamma^{(I)}$ Frequency Distributions

The four panels of Fig. 26 show the effect of relativistic kinematics on the $E_{\rm iso}$ frequency distribution of $\delta = 8$ power-law jets — see Eq. (18). Again, the "bare" ($\gamma \to \infty$) distribution is shown by a light solid line, whose slope in this case is -1/8.

The large value of δ has finally made it possible for this distribution to become relatively shallow and broad, possibly doing less violence to the observed, nearly-uniform distribution than was possible using shallower power-law indexes. It remains the case that the "needle jet" regime $\theta_0 \ll \gamma^{-1}$ must be avoided to avoid introducing too great a non-uniformity (see Eq. (32). This is likely to place a lower bound on $\gamma\theta_0$ in fits to the $E_{\rm iso}$ distribution data.

The four panels of Fig. 27 show the effect of relativistic kinematics on the $E_\gamma^{(I)}$ frequency distribution of $\delta = 8$ power-law jets — Eq. (19). Again, the "bare" ($\gamma \to \infty$) distribution is shown by a light solid line, whose slope in this case is -1/7.

Here the case is reversed. The "bare" slope is far too shallow, compared to the strongly-peaked distribution of the real data. It seems unlikely that relativistic kinematics in the "needle jet" regime can save the day, since even ignoring the just-discussed deleterious effect of this regime on the $E_{\rm iso}$ frequency distribution, the sharpest slope that can be produced in this regime is -1/2, by Eq. (33), which seems somewhat less steep than is consistent with the data.

4.5. Emission From Top-Hat Jet Profiles

4.5.1. Emission

The four panels of Fig. 28 show the behavior of $E_{\rm iso}$ as a function of viewing angle θ_v for a top-hat profile. We see jet broadening again, as expected.

The four panels of Fig. 29 show the behavior of $\langle D \rangle$ as a function of viewing angle θ_v. There is no "shelf" effect here, in contrast to the Fisher and the $\delta = 8$ power-law cases — the sharp edge of the profile is the feature that dominates the emission for $\gamma^{-1} < \theta_0$. One curiosity is the small "horn" structure that appears at the edge of the profile when $\gamma^{-1} < \theta_0$. For example, the curve for $\theta_0 = 0.03$, $\gamma^{-1} = 0.003$ (top right panel) shows a brief upswing of $\langle D \rangle$ just before it plummets off the edge. This feature is easily explained: $\langle D \rangle$ represents an average of the Doppler factor weighted by the Doppler photon distribution function. Both the Doppler factor and the Doppler photon distribution function peak along the line-of-sight. Over most of the face of the profile, the value of the average Doppler factor is dragged down

from the value at the peak by the lower values corresponding to photons arriving from off the line-of-sight. However, within γ^{-1} of the edge of the jet, some of the photons that perform this "dragging down" office are simply missing, so the average briefly surges up.

4.5.2. $E_{iso} - \langle D \rangle$ and $E_{\gamma}^{(I)} - \langle D \rangle$ Correlations

The four panels of Fig. 30 show the behavior of the E_{iso}–$\langle D \rangle$ ("Amati") correlation in universal top-hat models. The axis scales are chosen so that a slope of 0.5 appears as a 45° line, in order to ease the search for an "Amati-like" slope.

As expected, the "needle jet" cases $\theta_0 \ll \gamma^{-1}$ exhibit the 1/3 slope characteristic of off-axis emission. These cases are therefore unpromising. The opposite case, $\theta_0 > \gamma^{-1}$ is more interesting. For example, in the case $\theta_0 = 0.1$, $\gamma^{-1} = 0.003$ (top left panel), the slope of the curve near the top is 0.46, and the gentler slope only sets in for fainter events. The similarity of the case $\theta_0 = 0.03$, $\gamma = 333$ (top right panel) to Figure 1 of Toma et al. (2005) (which assumed $\theta_0 = 0.02$, $\gamma^{-1} = 300$ is quite striking, particularly in view of of the contrast between the rather detailed nature of the Toma et al. (2005) model and the rather simple model presented here.

Potentially troubling is the fact that all the events seen on-axis are located at the tip of the hook structure at the end of the curve (this structure is a side-effect of the "horn" structure remarked upon in the previous section). Therefore, fits of this model to "Amati"-type data must constrain θ_0 to be small enough as not to overload the top end of the Amati relation with an excessive concentration of events. Note also that in order to take this profile seriously in a universal model, it is necessary to abandon the "GRBs are on-axis, XRFs are off-axis" paradigm of Yamazaki et al. (2002, 2003), since otherwise only XRFs would obey the Amati relation, while all GRBs would cluster very tightly in the E_{iso}-E_{peak} plane.

The four panels of Fig. 31 show the behavior of the $E_{\gamma}^{(I)}$–$\langle D \rangle$ ("Ghirlanda") correlation in universal top-hat models.

On the rising slope part of these curves, it appears that "Ghirlanda"-like slopes can indeed be made for $\gamma^{-1} < \theta_0$. As was the case for the Amati relation, the delicacy required to prevent a conspicuous blob of on-axis events from distorting the plot must necessarily constrain θ_0.

4.5.3. E_{iso} and $E_\gamma^{(I)}$ Frequency Distributions

The four panels of Fig. 32 show the effect of relativistic kinematics on the E_{iso} frequency distribution of top-hat jets.

Here is evident the main difficulty that inheres in these models: the distribution of $dN/d\log E_{\mathrm{iso}}$ simply can not be made even approximately uniform, as required by the data. Rather, for most of the dynamic range $dN/d\log E_{\mathrm{iso}} \sim E_{\mathrm{iso}}^{-1/3}$, as expected for off-axis emission (Eq. 32). The distribution then piles up at the top of the E_{iso} range, where all the events that are viewed on-axis reside. It is apparent that no choice of parameters can make this model even remotely resemble the E_{iso} frequency data.

The four panels of Fig. 33 show the effect of relativistic kinematics on the $E_\gamma^{(I)}$ frequency distribution of top-hat jets.

The curious, two-peak structure observed in some of these curves is produced by the application of the Frail et al. (2001) prescription to top-hat profiles, in conjunction with the discontinuous nature of the break angle, $\theta_{br} = \max(\theta_v, \theta_0)$. A spike can appear near the energy corresponding to θ_0, since the functional dependence of $E_\gamma^{(I)}$ on θ_v can produce a maximum there, which produces a spike in the distribution function by Eq. (30).

Events viewed near- or on-axis (the "spiky" components) appear capable of producing relatively narrow $E_\gamma^{(I)}$ frequency distributions, especially for $\gamma^{-1} < \theta_0$. The case of $\theta_0 = 0.1$, $\gamma^{-1} = 0.003$ (top left panel) is an example. In this case, however, one must write off the off-axis component, which is undeniably broad, perhaps under cover of the fact that these would be XRFs, and cannot at present be placed in a "Ghirlanda"-type plot, since no break times have yet been observed for XRFs with redshifts.

5.   Discussion

From the foregoing exploration, it appears that relativistic kinematics cannot alleviate the weakness of universal jet models that we identified in §2.4: it does not appear possible for a universal jet model to produce a narrow distribution of $E_\gamma^{(I)}$ simultaneously with a broad distribution of E_{iso}. This is a difficulty for universal jets, although not necessarily a fatal one. The currently-available sample of $E_\gamma^{(I)}$ values is certainly more strongly affected by systematic selection effects than the sample of E_{iso} values, since there is some fraction of bursts for which no jet break is known. In particular, there are no jet breaks available for X-Ray Flash events, so that the frequency distribution of $E_\gamma^{(I)}$ may in fact extend to XRFs, despite being truncated by observational selection effects. Nonetheless, even concentrating

only on GRBs, it is striking that the empirical width of the $E_\gamma^{(I)}$ distribution of GRBs is is not much larger than a single decade, while the width of the E_{iso} distribution is somewhere between three and four decades. It is hard to understand how such a discrepancy could be produced by selection effects alone.

There is a generic effect of relativistic kinematics that is worth highlighting: The relativistic beaming angle γ^{-1} imposes a lower limit on the effective angular size of the jet. Underlying jet emission profiles that are narrower than γ^{-1} will be broadened to an angular size of γ^{-1} by the relativistic Doppler effect. This effect has been noted in the case of afterglow emission (Woods & Loeb 1999; Rossi et al. 2002), but its influence on prompt emission has not been widely discussed. The net effect is to impose an upper bound on the extent to which the prompt flux can be amplified by collimation of the profile. A concomitant effect is to curb the ability of very steep profiles to produce a large dynamic range of emission intensity.

It seems worth commenting further upon the "shelf" feature of the $\langle D \rangle - \theta_v$ plots that was examined carefully in the case of Fisher jet profiles, and remarked upon in the case of $\delta = 8$ power-law profiles. This feature appears to be a generic property of steep profiles, as might be expected from the explanation provided in §4.1.1. It illustrates the fact that relativistic kinematics can not only serve to soften a source spectrum (as is the case for the spectrum emitted by a narrow jet observed far off-axis), but can also *harden* a GRB spectrum with respect to what might be expected from a naive application of "needle-jet" kinematics. For example, in the case of a Fisher jet with $\theta_0 = 0.1$, one might naively expect that for $\theta_v > \theta_0$, the jet profile presents the appearance of a needle jet, so that $\langle D \rangle$ must drop away as $(1 - \beta \mu_v)^{-1}$. It is therefore surprising to find that $\langle D \rangle$ can in fact remain relatively constant and considerably higher than this naive argument would lead us to believe, even quite far from the jet axis.

It is encouraging to note that Amati-like and Ghirlanda-like correlations may emerge from "steep" profiles such as the Fisher profile, or the $\delta = 8$ power-law profile, under suitable choices of θ_0 and γ. It is somewhat striking, even surprising, to find such correlations emerging of their own accord from top-hat profiles. Such profiles are not usually considered promising candidates for universal models, as they are not "structured". The main exception to this view has been put forward by Yamazaki and collaborators (Yamazaki et al. 2002, 2003, 2004; Toma et al. 2005), as well as other papers by the same authors. It is certainly proven to be something of a surprise that top-hat models can produce Amati slopes much steeper than the 1/3 value expected from a relativistic point source (the "needle jet" approximation).

It is noteworthy that in the case of the jet profiles that have a decent chance of making realistic-looking Amati/Ghirlanda relations (the Fisher profile, the $\delta = 8$ power-law profile,

and the top-hat profile), it is invariably the case that the Ghirlanda relation has a steeper slope than the Amati relation. This steepening is evidently a purely geometrical effect. It is clearly unrelated to the steepening effect noticed by Levinson & Eichler (2005), since we have certainly not included any dependency of the break angle on $E_{\rm iso}$, the source of the steepening noted in that paper. Apparently, with a break angle that is conceived purely in terms of geometry, it is still the case that Ghirlanda relations of universal models are expected to be steeper than their corresponding Amati relations.

The inability of shallow power-law profiles ($\delta = 1$ and $\delta = 2$) to produce any substantial dynamic range in $\langle D \rangle$ spells major trouble for such models, above and beyond their expected inability to produce broad $E_{\rm iso}$ distributions. This aspect of the situation might be correctable, if one is willing to incur the cost of introducing an angular dependence of the spectrum, in conjunction with the angular dependence of the emission profile. In particular, one could consider the (purely empirical) introduction of a relation like $E_{\rm peak} \propto \epsilon(\vec{n} \cdot \vec{b})^{1/2}$ as a microphysical relation satisfied on the surface of the shock.

There have been some investigations that appear at first glance to do something like this. Yamazaki et al. (2004) introduced an intrinsic Amati relation between $E_{\rm peak}$ and $E_{\rm iso}$ in their universal off-axis model, to examine how the correlation was modified by relativistic kinematics for off-axis observers. Zhang et al. (2004) similarly assumed an intrinsic Amati relation in their study of Gaussian jet profiles.

Kobayashi et al. (2002) pointed out that $E_{\rm peak}^{2}$ is proportional to the internal energy of the jet material. Zhang & Mészáros (2002b) and Ramirez-Ruiz & Lloyd-Ronning (2002) observed that internal synchrotron models can certainly produce a correlation between $E_{\rm peak}$ and the luminosity, although the exact shape of the correlation varies with the dependence of L on γ. It should be pointed out, however, that these dependencies of luminosity on $E_{\rm peak}$ appear to be "global" statements about average conditions prevailing in the jet. The question of whether an internal shock model radiating by synchrotron emission might be expected to exhibit a *local* Amati-like correlation between $E_{\rm peak}$ and emissivity has not, to our knowledge, been addressed.

We note in passing that it would be straightforward to modify our method to calculate $E_{\rm peak}$ instead of $\langle D \rangle$ in such a model, since all that is necessary is to introduce an additional multiplicative function $E_{\rm peak}(\vec{n} \cdot \vec{b})$ in the integral in the numerator of Eq. (26).

REFERENCES

Amati, L., et al. 2002, A&A, 390, 81

Band, D., et al. 1993, ApJ, 413, 281

Bloom, J. S., Frail, D. A., & Kulkarni, S. R. 2003, ApJ, 594, 674

Cooley, J. W., and Tukey, J. W. 1965, Math. Comput. 19, 297

Gradshteyn, I. S., and Rhyzik, I. M. 1965, Tables of Integrals, Series, and Products (New York: Academic)

Dai, X., and Zhang, B. 2005, ApJ 621, 875

Driscoll, J. R, and Healy, D. M. 1994, Adv. Appl. Math. 15, 202

Frail, D. A. et al 2001, ApJ 562, L55

Ghirlanda, G., Ghisellini, G., & Lazzati, D. 2004, ApJ, 616, 331

Heise, J., in't Zand, J., Kippen, R. M., & Woods, P. M. 2001, Gamma-ray Bursts in the Afterglow Era, 16

Kippen, R. M., Woods, P. M., Heise, J., in't Zand, J., Preece, R. D., & Briggs, M. S. 2001, Gamma-ray Bursts in the Afterglow Era, 22

Granot, J., Piran, T., & Sari, R. 1999, ApJ, 513, 679

Granot, J., & Kumar, P. 2003, ApJ, 591, 1086

Kobayashi, S., Ryde, F., & MacFadyen, A. 2002, ApJ, 577, 302

Kumar, P., & Granot, J. 2003, ApJ, 591, 1075

Guetta, D., Granot, J., & Begelman, M. C. 2005, ApJ, 622, 482

Lapenta, G., & Kronberg, P. P. 2005, ApJ, 625, 37

Lamb, D. Q., et al. 2004, New Astronomy Review, 48, 423

Lamb, D. Q., Donaghy, T. Q., Graziani, C. 2005, ApJ620, 355-378

Levinson, A., and Eichler, D. 2005, astro-ph/0504125

Lloyd-Ronning, N. M., Dai, X., & Zhang, B. 2004, ApJ, 601, 371

Mardia, K. V. 1972, Statistics of Directional Data (New York: Academic)

Oh, S. P., Spergel, D. N., and Hinshaw, G. 1998, ApJ 510, 551

Piran, T. 1999, Phys. Rep., 314, 575

Ramirez-Ruiz, E., & Lloyd-Ronning, N. M. 2002, New Astronomy, 7, 197

Rees, M. J., & Mészáros, P. 1994, ApJ, 430, L93

Rhoads, J. E. 1999, ApJ, 525, 737

Rossi, E., Lazzati, D., & Rees, M. J. 2002, MNRAS, 332, 945

Sari, R., Piran, T., & Halpern, J. P. 1999, ApJ, 519, L17

Stern, B. E. 2003, MNRAS, 345, 590

Toma, K., Yamazaki, R., and Nakamura, T. 2005, astro-ph/0504624

Wandelt, B. D., and Górski, K. M 2001, Phys. Rev. D, 63, 123002

Woods, E., & Loeb, A. 1999, ApJ, 523, 187

Yamazaki, R., Ioka, K., & Nakamura, T. 2002, ApJ, 571, L31

Yamazaki, R., Ioka, K., & Nakamura, T. 2003, ApJ, 593, 941

Yamazaki, R., Ioka, K., and Nakamura, T. 2004, ApJ 606, L33

Zhang, B., Dai, X., Lloyd-Ronning, N. M., & Mészáros, P. 2004, ApJ, 601, L119

Zhang, B., and Mészáros, P. 2002, ApJ 571, 876

Zhang, B., & Mészáros, P. 2002, ApJ, 581, 1236
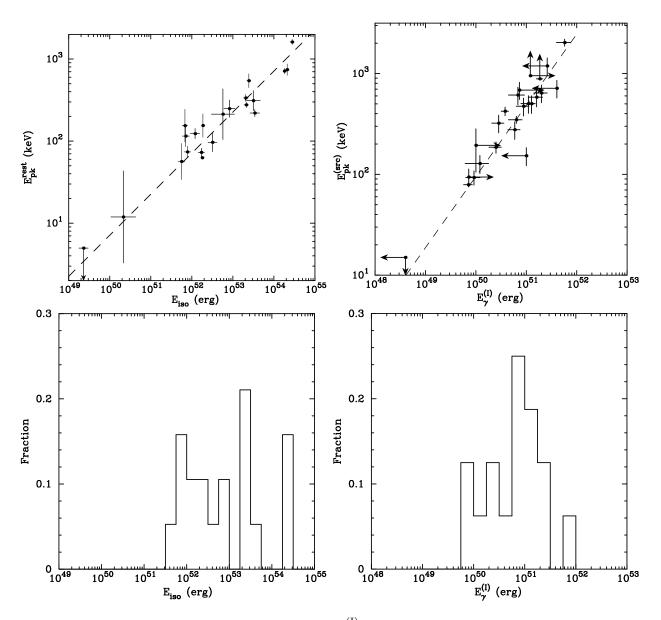
Fig. 1.— Empirical properties of E_{iso} and $E_\gamma^{(\mathrm{I})}$. Top left: Amati relation. Top right: Ghirlanda relation. Bottom left: Histogram of E_{iso} values, excluding XRFs. Bottom right: Histogram of $E_\gamma^{(\mathrm{I})}$ values for events with well-determined $E_\gamma^{(\mathrm{I})}$. The data used to make the plots in the left-hand panels is from Lamb et al. (2004). The data used to make the plots in the right-hand panels is from Ghirlanda et al. (2004).
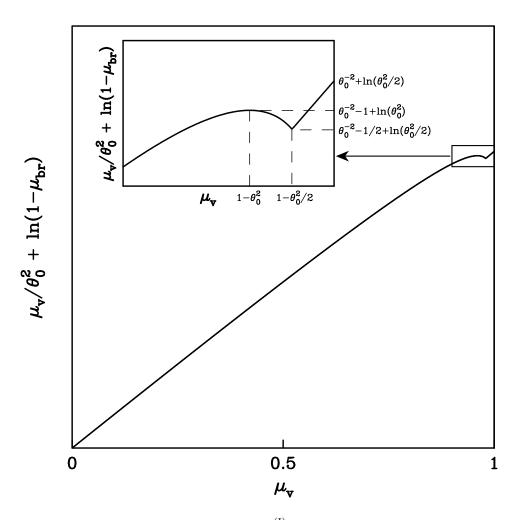
Fig. 2.— Graphical analysis of the $E_\gamma^{(I)}$ distribution of Universal Fisher jets.
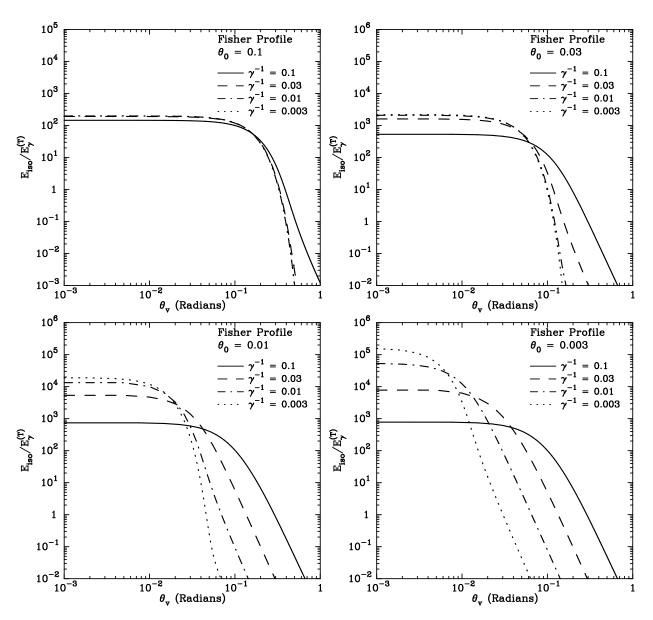
Fig. 3.— E_{iso} as a function of viewing angle for emission from relativistic jets with Fisher emission profiles. Each panel shows the result for $\gamma^{-1} = 0.1$, 0.03, 0.01, and 0.003. Top left: $\theta_0 = 0.1$. Top right: $\theta_0 = 0.03$. Bottom left: $\theta_0 = 0.01$. Bottom right: $\theta_0 = 0.003$.
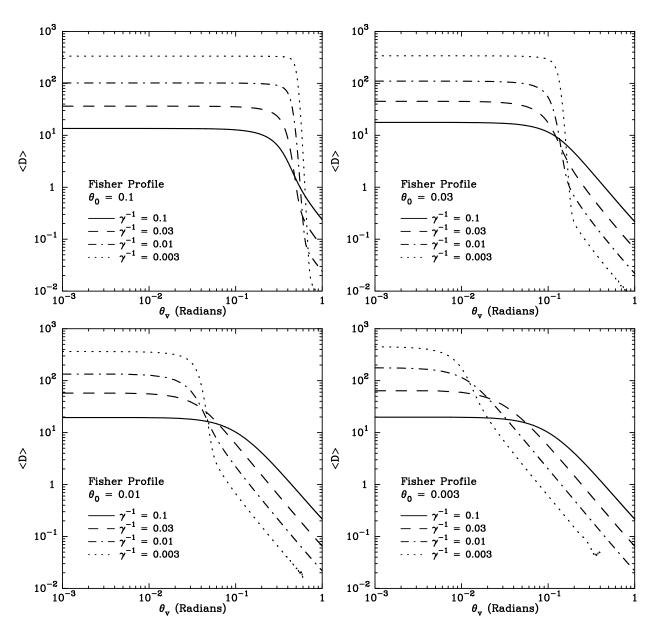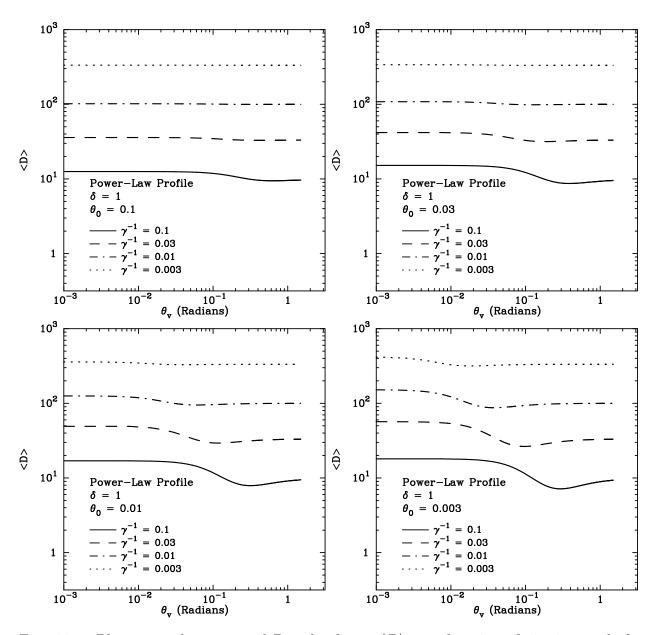
Fig. 4.— Photon-number-averaged Doppler factor $\langle D \rangle$ as a function of viewing angle for emission from relativistic jets with top-hat emission profiles. Each panel shows the result for $\gamma^{-1} = 0.1$, 0.03, 0.01, and 0.003. Top left: $\theta_0 = 0.1$. Top right: $\theta_0 = 0.03$. Bottom left: $\theta_0 = 0.01$. Bottom right: $\theta_0 = 0.003$. Note the curious "shelf" behavior for $\gamma^{-1} \ll \theta_0$.
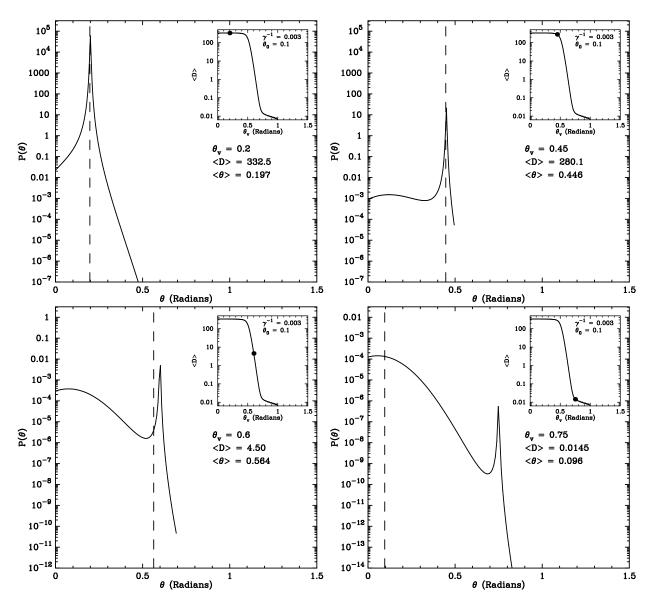
Fig. 5.— Photon provenance distributions for a Fisher jet with $\gamma^{-1} = 0.003$, $\theta_0 = 0.1$. These plots illustrate the origin of the "shelf" behavior in the profile of $\langle D \rangle$, as seen in Fig. 4. Top left: $\theta_v = 0.2$. Top right: $\theta_v = 0.45$. Bottom left: $\theta_v = 0.6$. Bottom right: $\theta_v = 0.75$. In each panel, the x-axis is angular location on the jet, while the y-axis is the (un-normalized) probability that a photon along θ_v should have been emitted from that part of the jet. The inset shows the current θ_v and $\langle D \rangle$, represented as a dot on the $\langle D \rangle$ profile (now shown with a linear angular scale). The vertical dashed line shows the "mean" $\langle \theta \rangle$ obtained from the current value of $\langle D \rangle$.
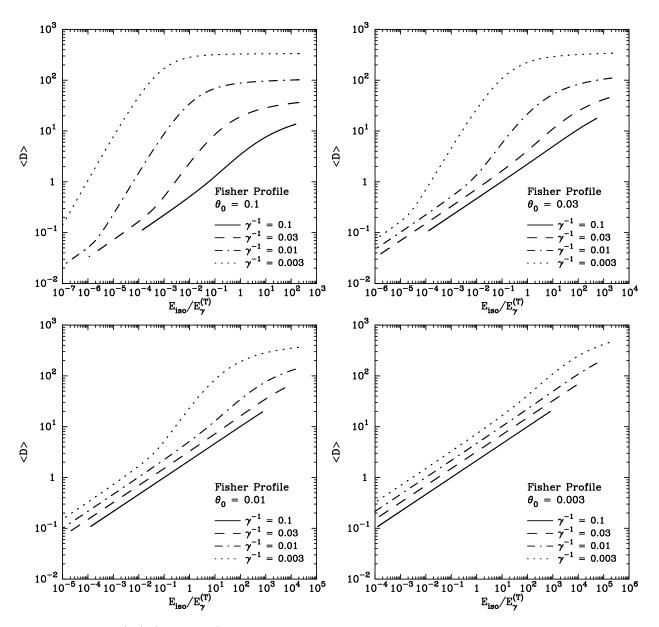
Fig. 6.— E_{iso}–$\langle D \rangle$ ("Amati") plots for universal jet models based on Fisher profiles. Each panel shows the result for $\gamma^{-1} = 0.1$, 0.03, 0.01, and 0.003. Top left: $\theta_0 = 0.1$. Top right: $\theta_0 = 0.03$. Bottom left: $\theta_0 = 0.01$. Bottom right: $\theta_0 = 0.003$.
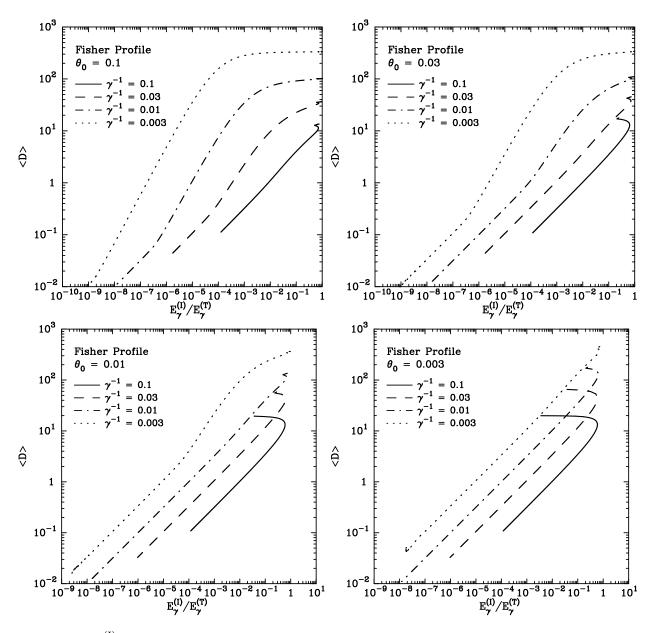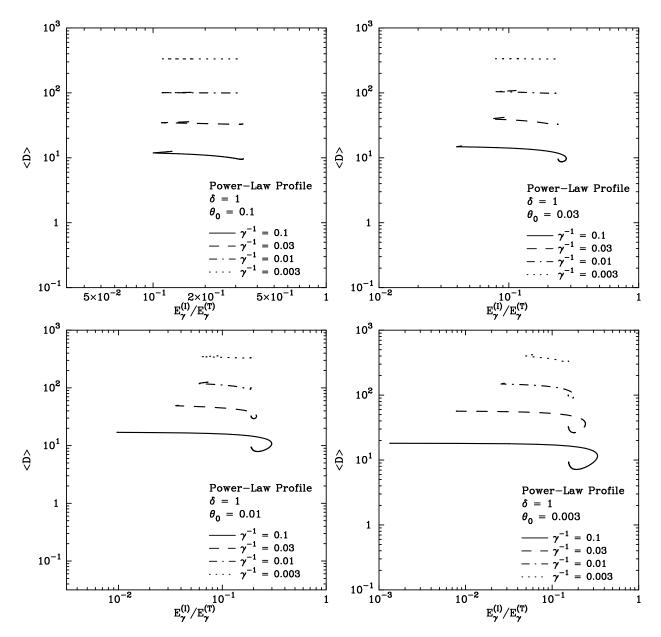
Fig. 7.— $E_\gamma^{(I)}$–$\langle D \rangle$ ("Ghirlanda") plots for universal jet models based on Fisher profiles. Each panel shows the result for $\gamma^{-1} = 0.1$, 0.03, 0.01, and 0.003. Top left: $\theta_0 = 0.1$. Top right: $\theta_0 = 0.03$. Bottom left: $\theta_0 = 0.01$. Bottom right: $\theta_0 = 0.003$.
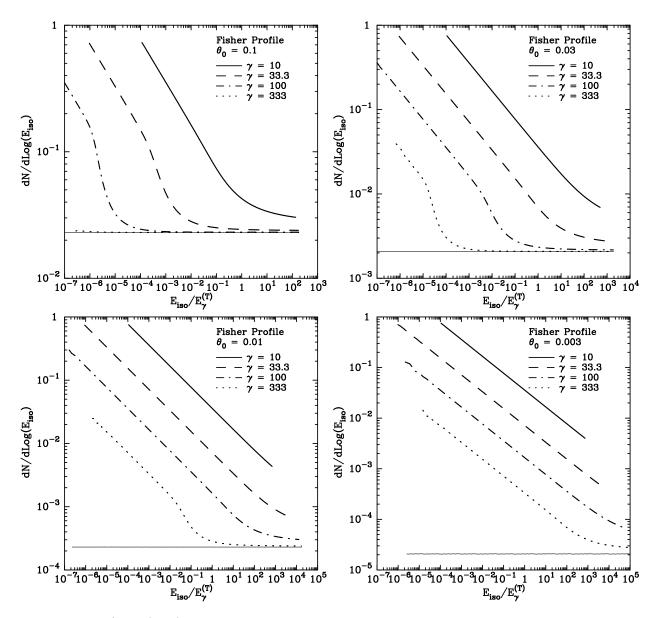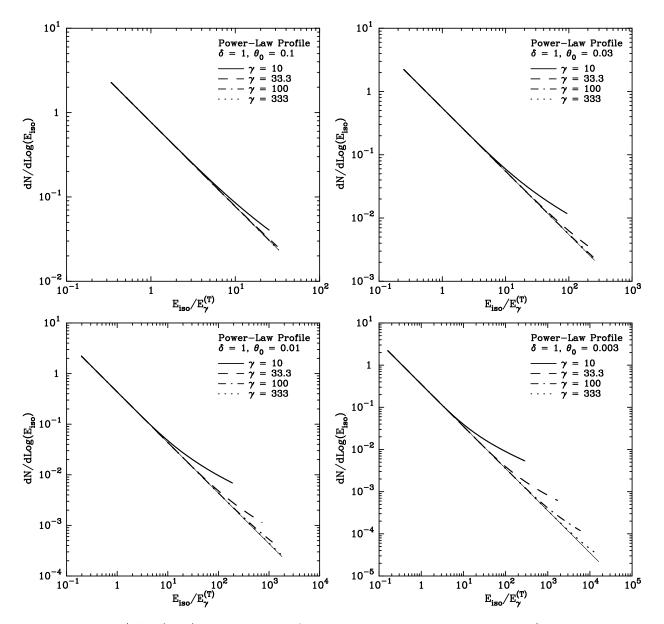
Fig. 8.— $dN/d\log(E_{\rm iso})$ distributions for universal jet models based on Fisher profiles. Each panel shows the result for $\gamma = 10$, 33.3, 100, and 333. Top left: $\theta_0 = 0.1$. Top right: $\theta_0 = 0.03$. Bottom left: $\theta_0 = 0.01$. Bottom right: $\theta_0 = 0.003$. The vertical scale is arbitrary. The horizontal light solid line shows the "bare" distribution due to the underlying profile — essentially the $\gamma \to \infty$ limit.
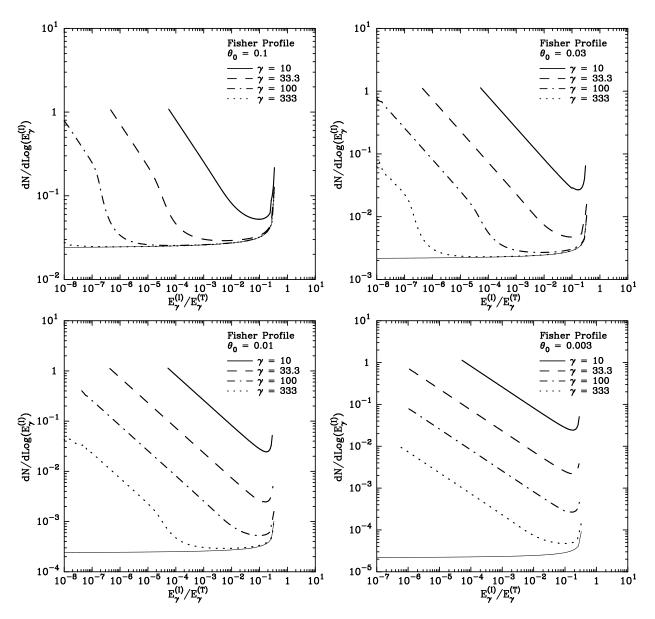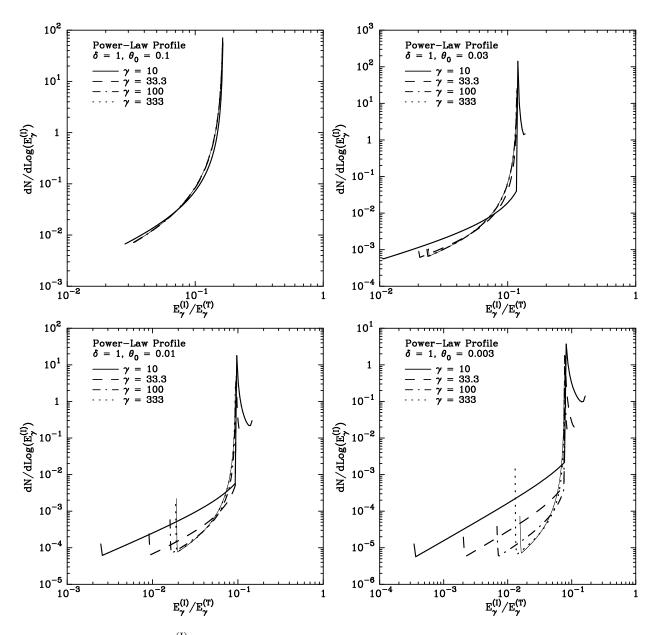
Fig. 9.— $dN/d\log(E_\gamma^{(I)})$ distributions for universal jet models based on Fisher profiles. Each panel shows the result for $\gamma = 10$, 33.3, 100, and 333. Top left: $\theta_0 = 0.1$. Top right: $\theta_0 = 0.03$. Bottom left: $\theta_0 = 0.01$. Bottom right: $\theta_0 = 0.003$. The vertical scale is arbitrary. The light solid line shows the "bare" distribution due to the underlying profile — essentially the $\gamma \to \infty$ limit.
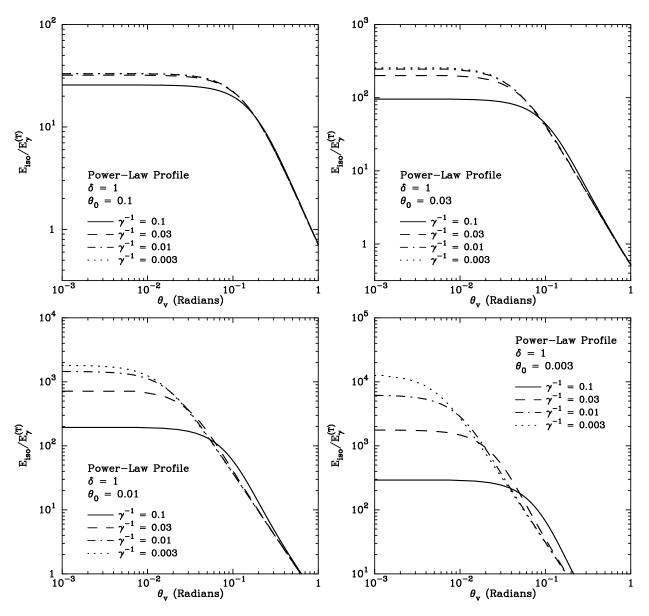
Fig. 10.— E_{iso} as a function of viewing angle for emission from relativistic jets with $\delta = 1$ power-law emission profiles. These figures help illustrate the fact that γ^{-1} sets a lower limit on the effective angular size of the jet. Each panel shows the result for $\gamma^{-1} = 0.1$, 0.03, 0.01, and 0.003. Top left: $\theta_0 = 0.1$. Top right: $\theta_0 = 0.03$. Bottom left: $\theta_0 = 0.01$. Bottom right: $\theta_0 = 0.003$.

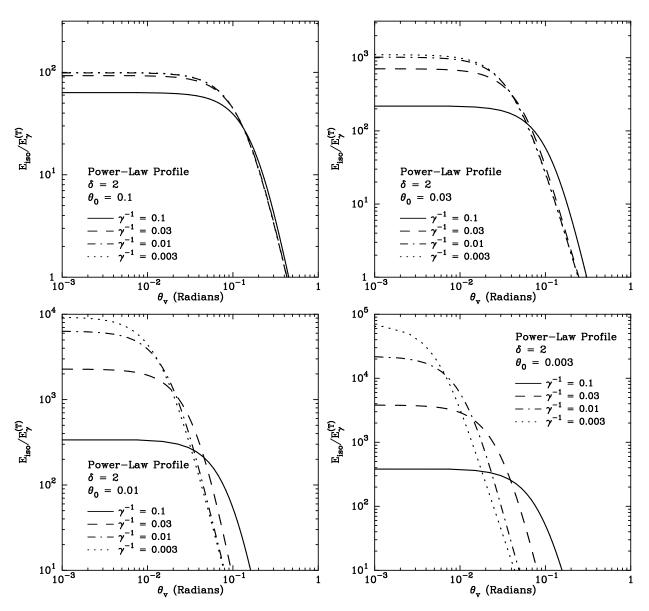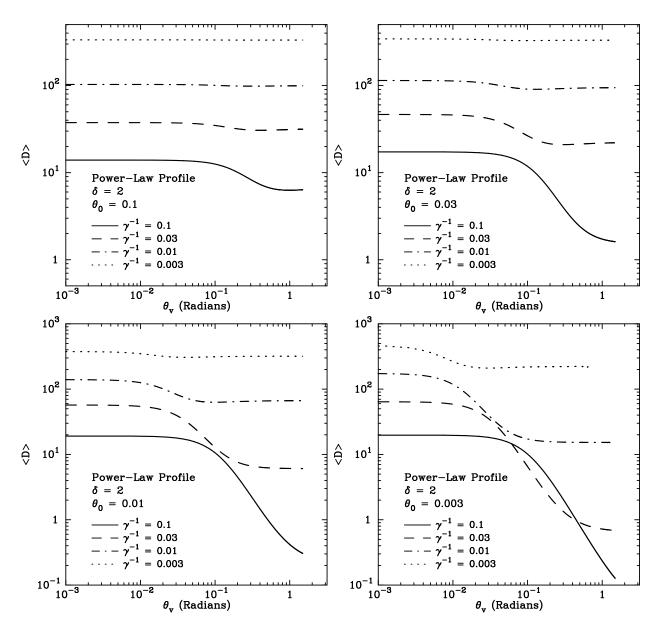Fig. 11.— Photon-number-averaged Doppler factor $\langle D \rangle$ as a function of viewing angle for emission from relativistic jets with $\delta = 1$ power-law emission profiles. Each panel shows the result for $\gamma^{-1} = 0.1$, 0.03, 0.01, and 0.003. Top left: $\theta_0 = 0.1$. Top right: $\theta_0 = 0.03$. Bottom left: $\theta_0 = 0.01$. Bottom right: $\theta_0 = 0.003$. At large θ_v, $\langle D \rangle \to \gamma$. It is noteworthy that the dynamic range of $\langle D \rangle$ is small compared to the other profiles we consider.
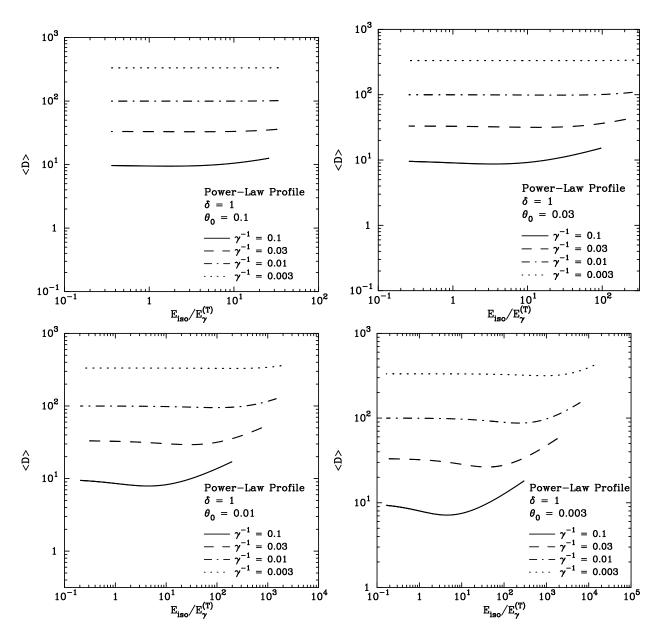
Fig. 12.— E_{iso}–$\langle D \rangle$ ("Amati") plots for universal jet models based on $\delta = 1$ power-law profiles. Each panel shows the result for $\gamma^{-1} = 0.1$, 0.03, 0.01, and 0.003. Top left: $\theta_0 = 0.1$. Top right: $\theta_0 = 0.03$. Bottom left: $\theta_0 = 0.01$. Bottom right: $\theta_0 = 0.003$.

Fig. 13.— $E_\gamma^{(I)}$–$\langle D \rangle$ ("Ghirlanda") plots for universal jet models based on $\delta = 1$ power-law profiles. Each panel shows the result for $\gamma^{-1} = 0.1$, 0.03, 0.01, and 0.003. Top left: $\theta_0 = 0.1$. Top right: $\theta_0 = 0.03$. Bottom left: $\theta_0 = 0.01$. Bottom right: $\theta_0 = 0.003$.
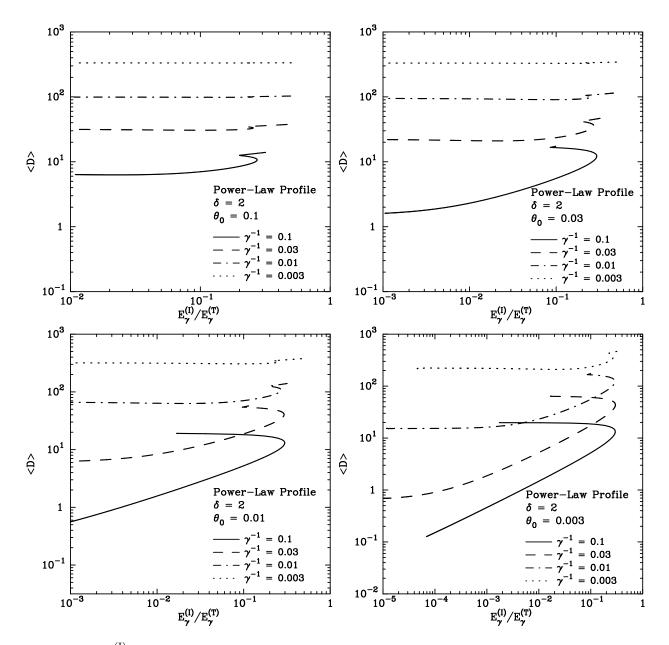
Fig. 14.— $dN/d\log(E_{\mathrm{iso}})$ distributions for universal jet models based on $\delta = 1$ power-law profiles. Each panel shows the result for $\gamma = 10, 33.3, 100,$ and 333. Top left: $\theta_0 = 0.1$. Top right: $\theta_0 = 0.03$. Bottom left: $\theta_0 = 0.01$. Bottom right: $\theta_0 = 0.003$. The vertical scale is arbitrary. The light solid line shows the "bare" distribution due to the underlying profile — essentially the $\gamma \to \infty$ limit. Its slope is -1, as expected from Eq. 18.

Fig. 15.— $dN/d\log(E_\gamma^{(I)})$ distributions for universal jet models based on $\delta = 1$ power-law profiles. Each panel shows the result for $\gamma = 10$, 33.3, 100, and 333. Top left: $\theta_0 = 0.1$. Top right: $\theta_0 = 0.03$. Bottom left: $\theta_0 = 0.01$. Bottom right: $\theta_0 = 0.003$. The vertical scale is arbitrary. The light solid line shows the "bare" distribution due to the underlying profile — essentially the $\gamma \to \infty$ limit. If it were not for the θ_0 cutoff and the relativistic kinematics, this distribution would be a δ-function, by construction.

Fig. 16.— $E_{\rm iso}$ as a function of viewing angle for emission from relativistic jets with $\delta = 2$ power-law emission profiles. Each panel shows the result for $\gamma^{-1} = 0.1$, 0.03, 0.01, and 0.003. Top left: $\theta_0 = 0.1$. Top right: $\theta_0 = 0.03$. Bottom left: $\theta_0 = 0.01$. Bottom right: $\theta_0 = 0.003$.

Fig. 17.— Photon-number-averaged Doppler factor $\langle D \rangle$ as a function of viewing angle for emission from relativistic jets with $\delta = 2$ power-law emission profiles. Each panel shows the result for $\gamma^{-1} = 0.1$, 0.03, 0.01, and 0.003. Top left: $\theta_0 = 0.1$. Top right: $\theta_0 = 0.03$. Bottom left: $\theta_0 = 0.01$. Bottom right: $\theta_0 = 0.003$. The dynamic range of $\langle D \rangle$ is still quite limited, for almost all of the selected parameters.
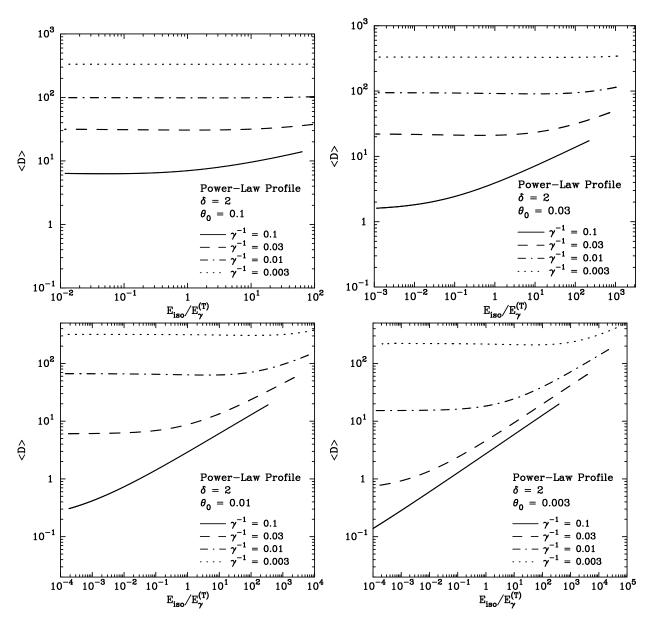
Fig. 18.— $E_{\rm iso}$–$\langle D \rangle$ ("Amati") plots for universal jet models based on $\delta = 2$ power-law profiles. Each panel shows the result for $\gamma^{-1} = 0.1$, 0.03, 0.01, and 0.003. Top left: $\theta_0 = 0.1$. Top right: $\theta_0 = 0.03$. Bottom left: $\theta_0 = 0.01$. Bottom right: $\theta_0 = 0.003$.

Fig. 19.— $E_\gamma^{(I)}$–$\langle D \rangle$ ("Ghirlanda") plots for universal jet models based on $\delta = 2$ power-law profiles. Each panel shows the result for $\gamma^{-1} = 0.1$, 0.03, 0.01, and 0.003. Top left: $\theta_0 = 0.1$. Top right: $\theta_0 = 0.03$. Bottom left: $\theta_0 = 0.01$. Bottom right: $\theta_0 = 0.003$.
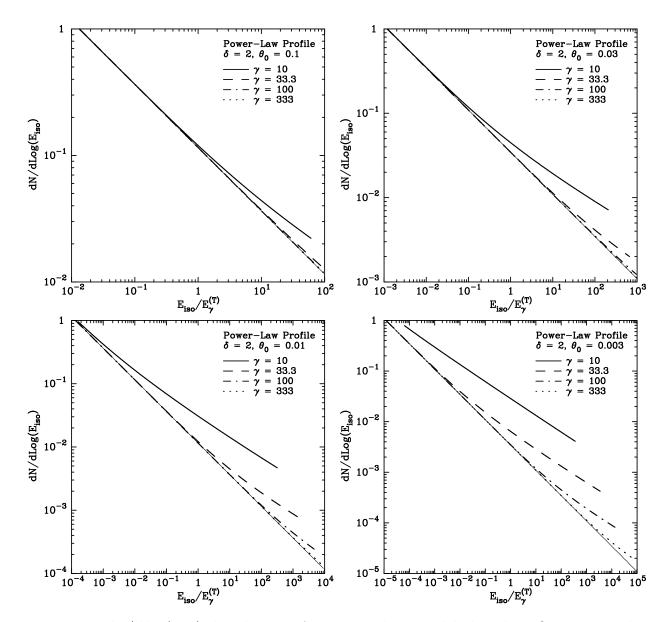
Fig. 20.— $dN/d\log(E_{\rm iso})$ distributions for universal jet models based on $\delta = 2$ power-law profiles. Each panel shows the result for $\gamma = 10$, 33.3, 100, and 333. Top left: $\theta_0 = 0.1$. Top right: $\theta_0 = 0.03$. Bottom left: $\theta_0 = 0.01$. Bottom right: $\theta_0 = 0.003$. The vertical scale is arbitrary. The light solid line shows the "bare" distribution due to the underlying profile — essentially the $\gamma \to \infty$ limit. Its slope is -1/2, as expected from Eq. 18.
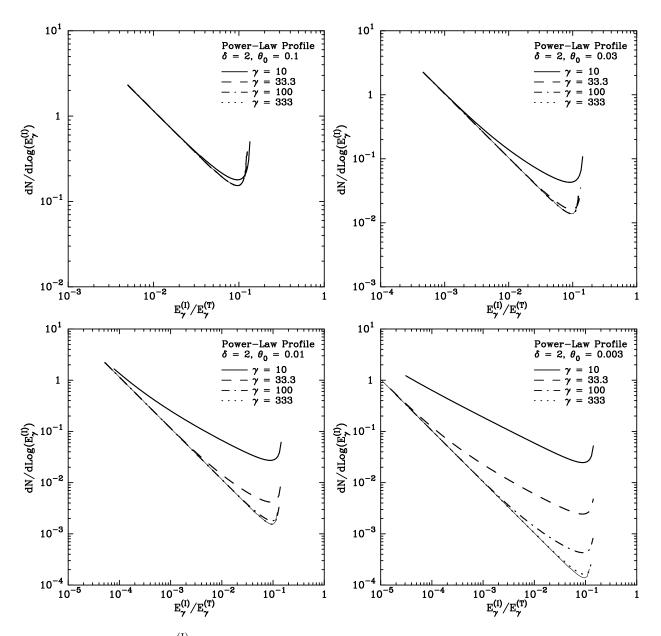
Fig. 21.— $dN/d\log(E_\gamma^{(I)})$ distributions for universal jet models based on $\delta = 2$ power-law profiles. Each panel shows the result for $\gamma = 10$, 33.3, 100, and 333. Top left: $\theta_0 = 0.1$. Top right: $\theta_0 = 0.03$. Bottom left: $\theta_0 = 0.01$. Bottom right: $\theta_0 = 0.003$. The vertical scale is arbitrary. The light solid line shows the "bare" distribution due to the underlying profile — essentially the $\gamma \to \infty$ limit. Its slope is -1, as expected from Eq. 19.
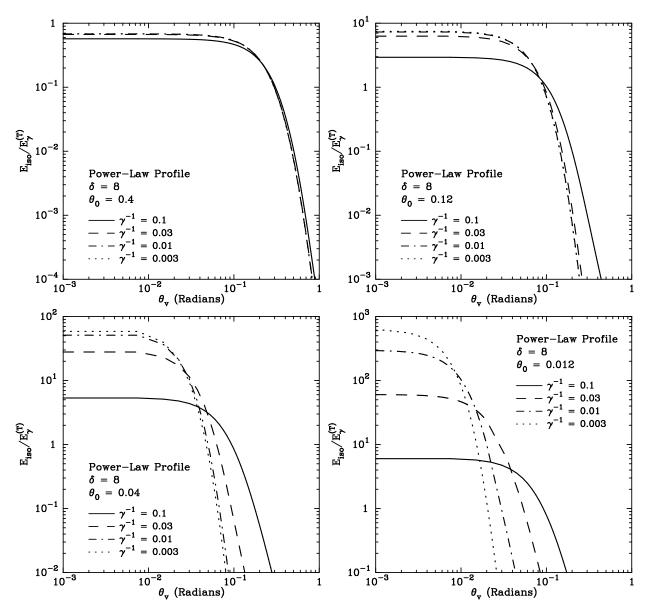
Fig. 22.— E_{iso} as a function of viewing angle for emission from relativistic jets with $\delta = 8$ power-law emission profiles. Each panel shows the result for $\gamma = 10$, 33.3, 100, and 333. Top left: $\theta_0 = 0.4$. Top right: $\theta_0 = 0.12$. Bottom left: $\theta_0 = 0.04$. Bottom right: $\theta_0 = 0.012$. These values of θ_0 are chosen so as to make the effective profile widths given by Eq. 44 be 0.1, 0.03, 0.01, and 0.003, respectively.
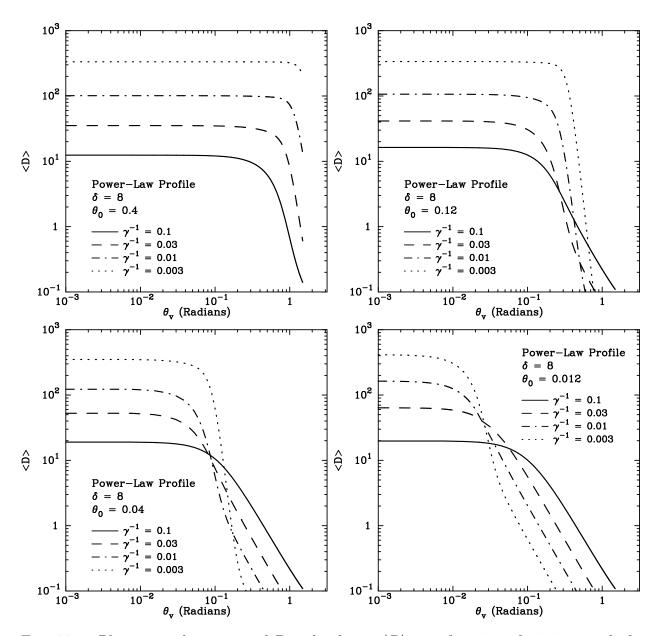
Fig. 23.— Photon-number-averaged Doppler factor $\langle D \rangle$ as a function of viewing angle for emission from relativistic jets with $\delta = 8$ power-law emission profiles. Each panel shows the result for $\gamma = 10$, 33.3, 100, and 333. Top left: $\theta_0 = 0.4$. Top right: $\theta_0 = 0.12$. Bottom left: $\theta_0 = 0.04$. Bottom right: $\theta_0 = 0.012$.
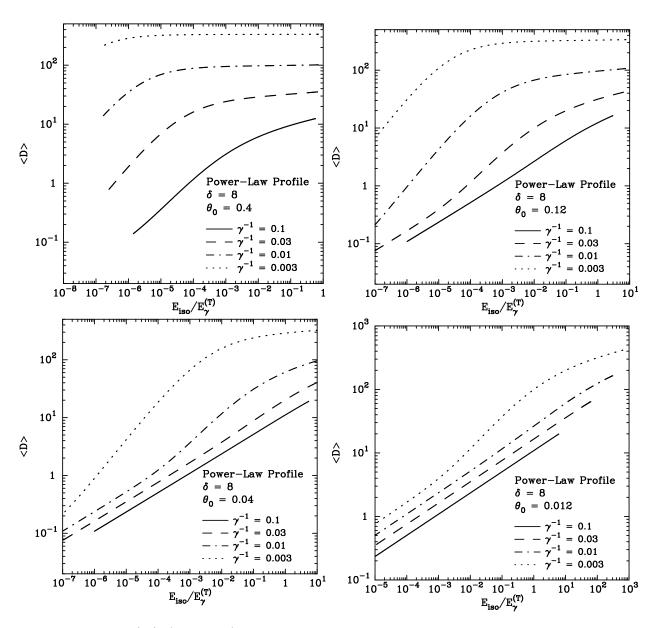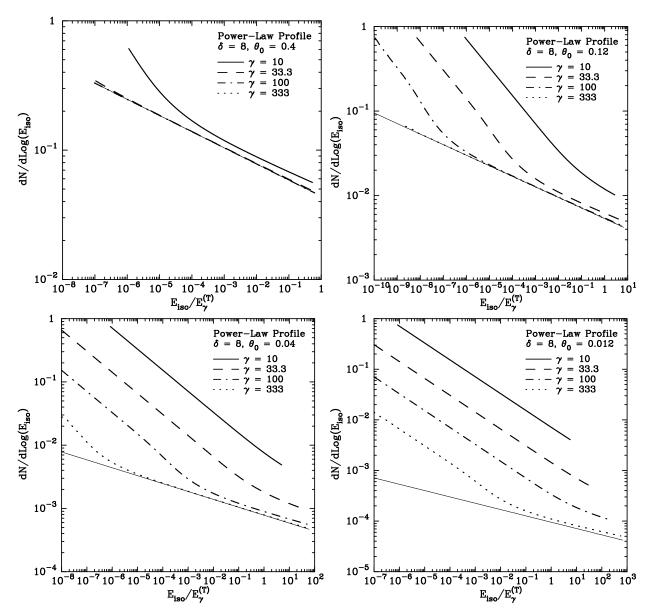
Fig. 24.— E_{iso}–$\langle D \rangle$ ("Amati") plots for universal jet models based on $\delta = 8$ power-law profiles. Each panel shows the result for $\gamma = 10, 33.3, 100,$ and 333. Top left: $\theta_0 = 0.4$. Top right: $\theta_0 = 0.12$. Bottom left: $\theta_0 = 0.04$. Bottom right: $\theta_0 = 0.012$.
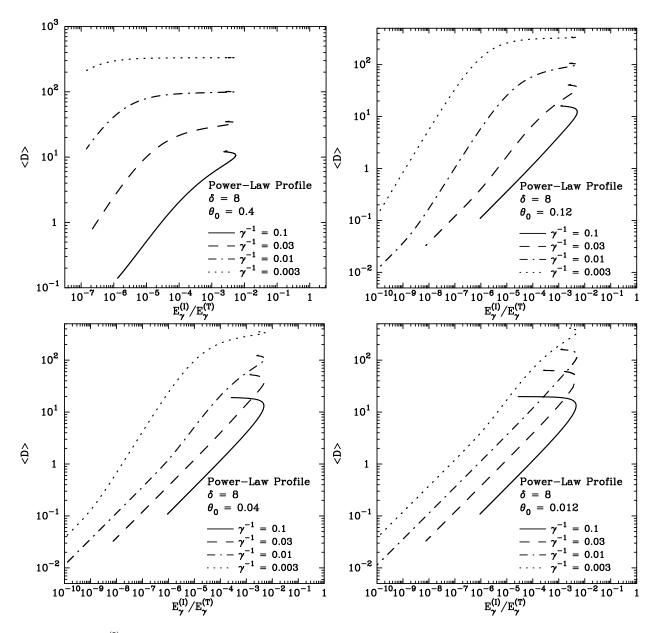
Fig. 25.— $E_\gamma^{(\mathrm{I})}$–$\langle D \rangle$ ("Ghirlanda") plots for universal jet models based on $\delta = 2$ power-law profiles. Each panel shows the result for $\gamma = 10, 33.3, 100,$ and 333. Top left: $\theta_0 = 0.4$. Top right: $\theta_0 = 0.12$. Bottom left: $\theta_0 = 0.04$. Bottom right: $\theta_0 = 0.012$.

Fig. 26.— $dN/d\log(E_{\mathrm{iso}})$ distributions for universal jet models based on $\delta = 8$ power-law profiles. Each panel shows the result for $\gamma = 10$, 33.3, 100, and 333. Top left: $\theta_0 = 0.4$. Top right: $\theta_0 = 0.12$. Bottom left: $\theta_0 = 0.04$. Bottom right: $\theta_0 = 0.012$. The vertical scale is arbitrary. The light solid line shows the "bare" distribution due to the underlying profile — essentially the $\gamma \rightarrow \infty$ limit. Its slope is -1/8, as expected from Eq. 18.
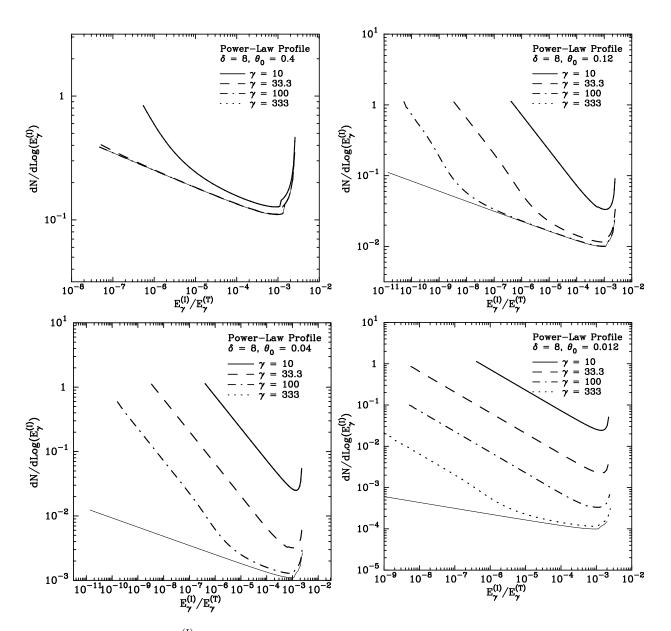
Fig. 27.— $dN/d\log(E_\gamma^{(I)})$ distributions for universal jet models based on $\delta = 8$ power-law profiles. Each panel shows the result for $\gamma = 10$, 33.3, 100, and 333. Top left: $\theta_0 = 0.4$. Top right: $\theta_0 = 0.12$. Bottom left: $\theta_0 = 0.04$. Bottom right: $\theta_0 = 0.012$. The vertical scale is arbitrary. The light solid line shows the "bare" distribution due to the underlying profile — essentially the $\gamma \to \infty$ limit. Its slope is -1/7, as expected from Eq. 19.
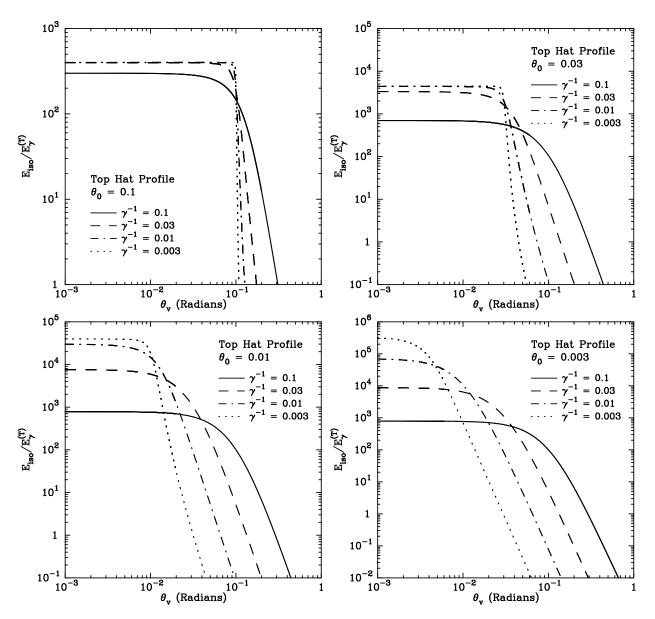
Fig. 28.— E_{iso} as a function of viewing angle for emission from relativistic jets with top-hat emission profiles. These figures help illustrate the fact that γ^{-1} sets a lower limit on the effective angular size of the jet. Each panel shows the result for $\gamma^{-1} = 0.1$, 0.03, 0.01, and 0.003. Top left: $\theta_0 = 0.1$. Top right: $\theta_0 = 0.03$. Bottom left: $\theta_0 = 0.01$. Bottom right: $\theta_0 = 0.003$.
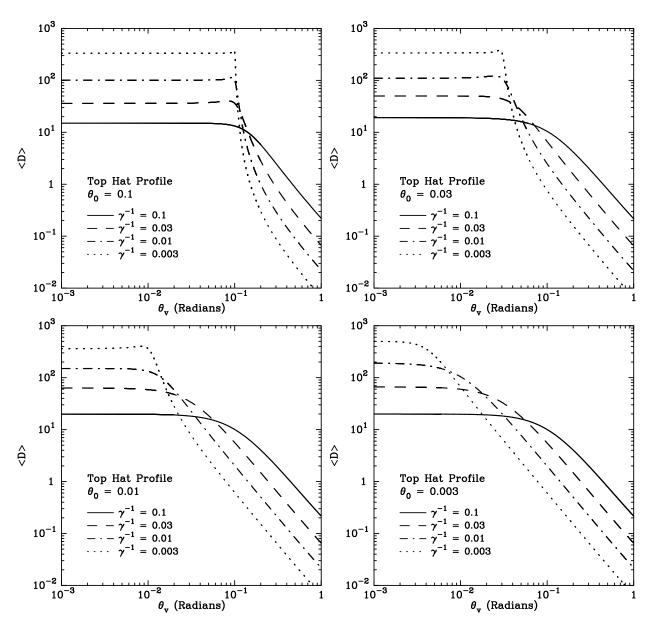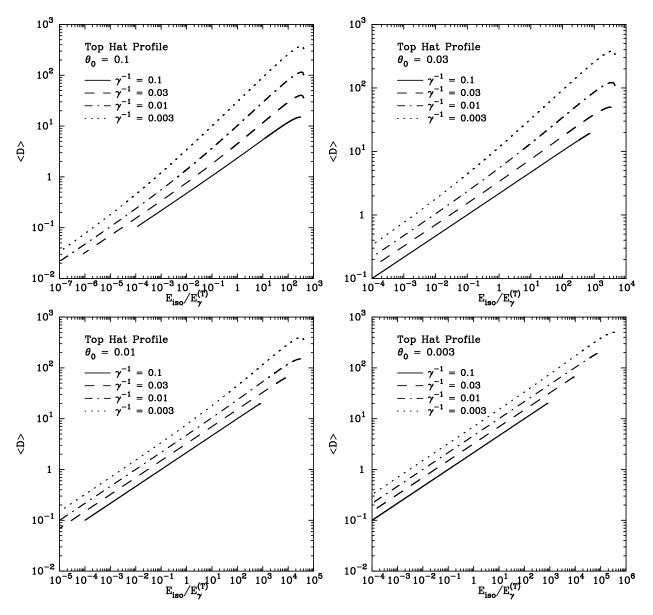
Fig. 29.— Photon-number-averaged Doppler factor $\langle D \rangle$ as a function of viewing angle for emission from relativistic jets with top-hat emission profiles. Each panel shows the result for $\gamma^{-1} = 0.1$, 0.03, 0.01, and 0.003. Top left: $\theta_0 = 0.1$. Top right: $\theta_0 = 0.03$. Bottom left: $\theta_0 = 0.01$. Bottom right: $\theta_0 = 0.003$.
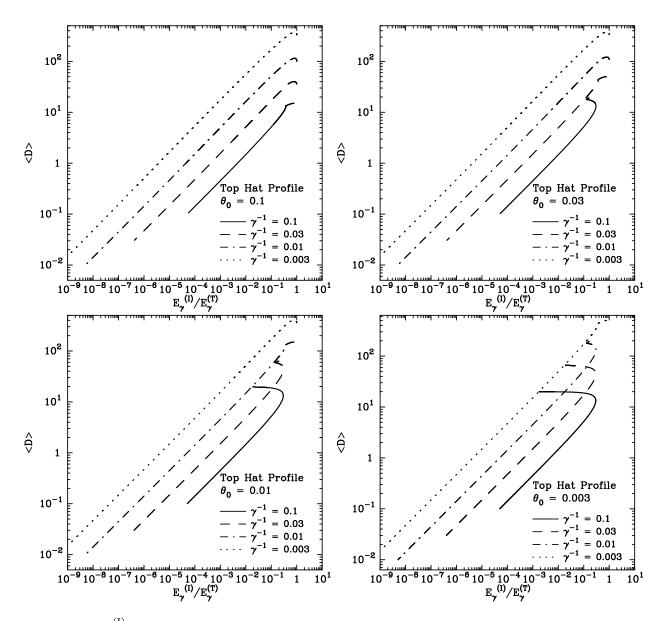
Fig. 30.— $E_{\rm iso}$–$\langle D \rangle$ ("Amati") plots for universal jet models based on top-hat profiles. Each panel shows the result for $\gamma^{-1} = 0.1$, 0.03, 0.01, and 0.003. Top left: $\theta_0 = 0.1$. Top right: $\theta_0 = 0.03$. Bottom left: $\theta_0 = 0.01$. Bottom right: $\theta_0 = 0.003$.

Fig. 31.— $E_\gamma^{(I)}$–$\langle D \rangle$ ("Ghirlanda") plots for universal jet models based on top-hat profiles. Each panel shows the result for $\gamma^{-1} = 0.1$, 0.03, 0.01, and 0.003. Top left: $\theta_0 = 0.1$. Top right: $\theta_0 = 0.03$. Bottom left: $\theta_0 = 0.01$. Bottom right: $\theta_0 = 0.003$.
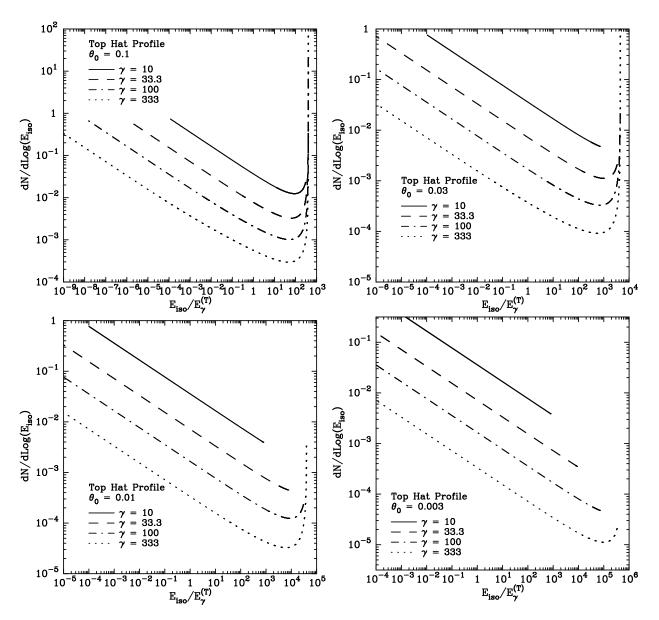
Fig. 32.— $dN/d\log(E_{\mathrm{iso}})$ distributions for universal jet models based on top-hat profiles. Each panel shows the result for $\gamma = 10$, 33.3, 100, and 333. Top left: $\theta_0 = 0.1$. Top right: $\theta_0 = 0.03$. Bottom left: $\theta_0 = 0.01$. Bottom right: $\theta_0 = 0.003$. The vertical scale is arbitrary.
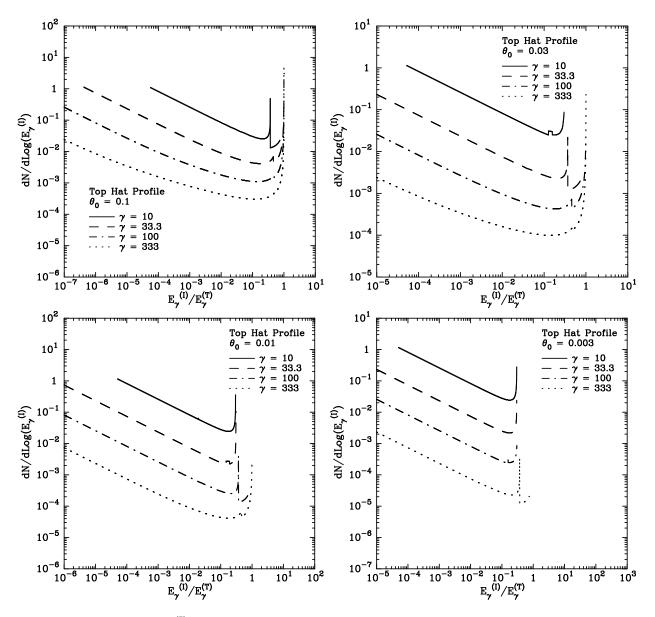
Fig. 33.— $dN/d\log(E_\gamma^{(\mathrm{I})})$ distributions for universal jet models based on top-hat profiles. Each panel shows the result for $\gamma = 10$, 33.3, 100, and 333. Top left: $\theta_0 = 0.1$. Top right: $\theta_0 = 0.03$. Bottom left: $\theta_0 = 0.01$. Bottom right: $\theta_0 = 0.003$. The vertical scale is arbitrary.